# JGR Solid Earth

# Ubiquitous Earthquake Dynamic Triggering in Southern California

**Nicolas D. DeSalvio[1]** and **Wenyuan Fan[1]**

[1]Scripps Institution of Oceanography, U.C. San Diego, La Jolla, CA, USA

**Abstract** Earthquakes can be dynamically triggered by the passing waves of other distant events. The frequent occurrence of dynamic triggering offers tangible hope in revealing earthquake nucleation processes. However, the physical mechanisms behind earthquake dynamic triggering have remained unclear, and contributions of competing hypotheses are challenging to isolate with individual case studies. To gain a systematic understanding of the spatiotemporal patterns of dynamic triggering, we investigate the phenomenon in southern California from 2008 to 2017. We use the Quake Template Matching catalog and an approach that does not assume an earthquake occurrence distribution. We develop a new set of statistics to examine the significance of seismicity-rate changes as well as moment-release changes. Our results show that up to 70% of 1,388 global $M \geq 6$ events may have triggered earthquakes in southern California. The triggered seismicity often occurred several hours after the passing seismic waves. The Salton Sea Geothermal Field, San Jacinto fault, and Coso Geothermal Field are particularly prone to triggering. Although adjacent fault segments can be triggered by the same earthquakes, the majority of triggered earthquakes seem to be uncorrelated, suggesting that the process is primarily governed by local conditions. Further, the occurrence of dynamic triggering does not seem to correlate with ground motion (e.g., peak ground velocity) at the triggered sites. These observations indicate that nonlinear processes may have primarily regulated the dynamic triggering cases.

**Plain Language Summary** Earthquakes interact with each other, such as mainshocks triggering nearby aftershocks. Earthquake dynamic triggering is a type of interaction where seismic waves from an earthquake trigger other earthquakes beyond several fault lengths, and sometimes, up to thousands of kilometers away. Triggered earthquakes may occur upon the arrival of the seismic waves but may also be delayed hours after the wave passage, suggesting the involvement of time-dependent processes. Identifying delayed cases relies on robust measures of seismicity-rate changes. Here we present a new method that can identify triggering cases without many assumptions. We find that earthquakes in southern California are frequently triggered by distant earthquakes around the globe, and the triggered earthquakes tend to cluster in space and time. We also find that the triggering incidences do not seem to correlate with the seismic wave characteristics of the distant earthquakes. Our findings suggest that dynamically triggered earthquakes in southern California are likely caused by time-dependent, local complex processes.

## 1. Introduction

While large earthquakes are difficult to predict on a given fault, earthquake occurrence is not completely random (e.g., Abercrombie & Mori, 1996; Ross, Idini, et al., 2019; Trugman & Ross, 2019; Utsu, 1961). Earthquakes interact with each other and often cluster in space and time, such as commonly observed mainshock-aftershock sequences. For example, the 1992 Landers earthquake caused widespread aftershocks that occurred in the near-field (Bosl & Nur, 2002; Harris & Simpson, 1992; Parsons & Dreger, 2000) and the far-field (Gomberg, 1996; Gomberg et al., 2001). The far-field aftershocks were likely triggered by the passing seismic waves, termed earthquake dynamic triggering (Aiken & Peng, 2014; Gomberg & Johnson, 2005; Gonzalez-Huizar & Velasco, 2011). As seismic waves pass through a region, transient dynamic stresses perturb local fault systems that ultimately trigger earthquakes (Hill & Prejean, 2015). This direct correlation between the triggered seismicity and passing waves reflects an observable process that promises tangible hope of deciphering earthquake nucleation mechanisms (Brodsky & van der Elst, 2014). Despite numerous observations of dynamic triggering around the globe, its occurrence conditions and associated precise physical mechanisms remain unclear (e.g., Fan et al., 2021; Meng & Peng, 2014; Velasco et al., 2008). Understanding the physical processes is crucial, as damaging earthquakes can be dynamically triggered (e.g., Pollitz et al., 2012; Uchide et al., 2016; Yoshida, 2016) but are not considered in most seismic hazard models (e.g., Field et al., 2014).

California is an ideal natural laboratory to study earthquake dynamic triggering because of its rich geophysical data sets including high-quality catalogs, seismic records, and geodetic observations. The long-term continuous records provide an opportunity to examine the phenomenon by comparing statistical observations to a variety of geophysical observables (e.g., Fan et al., 2021; Miyazawa et al., 2021). Dynamic triggering has been frequently observed in California following M7 earthquakes from different regions (e.g., Aiken & Peng, 2014; Fan et al., 2022; Kane et al., 2007; Meng & Peng, 2014; Prejean et al., 2004). Further, geothermal and volcanic areas in the region, such as the Salton Sea Geothermal Field (e.g., Fan et al., 2021), Coso Geothermal Field (e.g., Aiken & Peng, 2014), Geysers Geothermal Field (e.g., Stark & Davis, 1996), and Long Valley Caldera (e.g., Brodsky & Prejean, 2005) seem to be particularly susceptible to dynamic triggering.

In practice, earthquake dynamic triggering is often identified using statistical methods that examine the significance of seismicity-rate changes following candidate trigger earthquakes (e.g., Marsan & Nalbant, 2005; Pankow & Kilb, 2020; Wyss & Marsan, 2011). If the changes are statistically significant, the local earthquakes are inferred to be triggered seismicity (e.g., Marsan & Nalbant, 2005; Pankow & Kilb, 2020; Wyss & Marsan, 2011). Such statistical exercises often assume that local earthquake occurrence is a random and independent process, following a Poissonian distribution (Marsan & Nalbant, 2005; Pankow & Kilb, 2020). However, this assumption is inaccurate for transient, triggered seismicity due to its correlated activity, small sample size, and short duration (e.g., Fan et al., 2021). Fan et al. (2021) experimented using a sampling method to identify statistically significant changes in seismicity-rate, although their statistics were formulated following the Poissonian assumption. Here we critically reevaluate the approach and develop a method free from the Poissonian assumption.

There are several families of statistics that have been used to evaluate seismicity-rate changes. We focus on the two most commonly used statistics, the $\beta$-statistic (Matthews & Reasenberg, 1988) and the $Z$-statistic (Habermann, 1983). We compute the statistics using a sampling approach that is free from the aforementioned Poissonian assumption. We further develop two additional statistics to investigate earthquake moment-release changes, the $\beta_m$-statistic and the $Z_m$-statistic, which can help identify anomalous occurrence of earthquakes with large magnitudes. The four test statistics were applied to southern California earthquakes to identify cases of dynamic triggering from 2008 to 2017. The statistical results are then compared with seismic waveform characteristics, including peak ground velocity (PGV), peak frequency, kinetic energy, and relative frequency content. We aim to provide a systematic way to investigate the physical mechanisms of earthquake dynamic triggering.

This study shares its general framework with Fan et al. (2021): seismicity-rate anomalies are identified by comparing to seismicity-rates of other time windows in the catalog instead of using analytical solutions. However, both the statistical formulation and practical implementations are different in the two studies. Additionally, this study investigates dynamic triggering in southern California while Fan et al. (2021) only focused on the San Jacinto fault and Salton Sea Geothermal Field. We evaluate the differences and similarities between the two methods in Section 2.3.

We find that dynamic triggering is common throughout southern California, and about 70% of global $M \geq 6$ earthquakes may have triggered seismicity in the region. Significant seismic moment-release is triggered less often, but 52% of the global earthquakes may have triggered anomalies. Triggering of both types, seismicity and moment-release, is widespread in southern California, albeit with strong spatial heterogeneities in their triggering frequency. For example, earthquakes at geothermal fields and the San Jacinto fault are frequently triggered, but triggering is rarely observed in the Los Angeles basin. The general triggering patterns are consistent regardless of the test statistic that is used to evaluate the cases. We observe no obvious correlations between the triggering pattern and instantaneous waveform metrics (e.g., PGV), suggesting that the transient dynamic stress is unlikely the primary control for the observed cases. Our findings suggest that dynamic triggering in southern California likely involves nonlinear, local time-dependent processes that may occur over hours to a day within tens of kilometers. We have also applied a suite of tests to comprehensively evaluate the method and have confirmed the robustness of the findings.

## 2. Data and Methods

### 2.1. Catalog and Waveform Data

To study dynamic triggering in southern California, we use the Quake Template Matching catalog (QTM) with a detection threshold of 12 times the median average deviation (MAD) for local seismicity (Ross, Trugman,
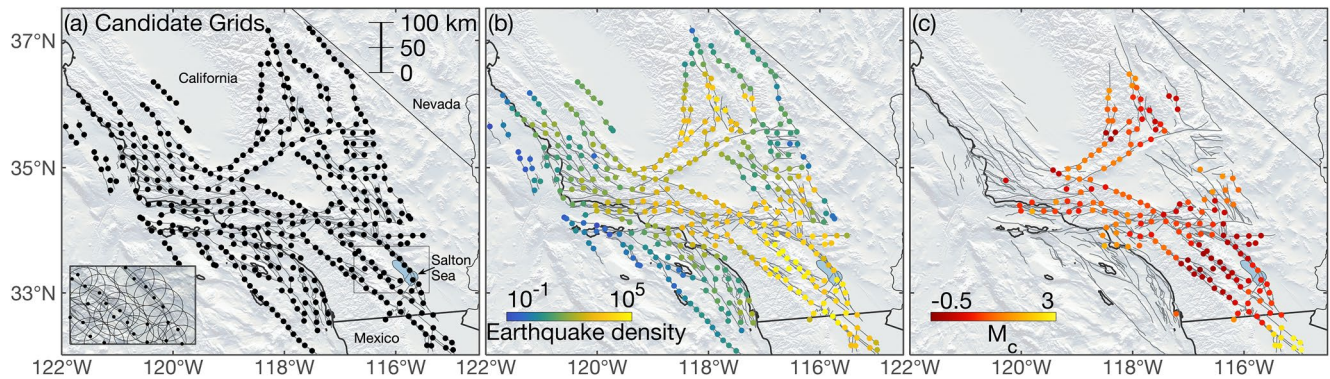
**Figure 1.** Study area in southern California. (a) Map of grid nodes where earthquake dynamic triggering is evaluated. Gray lines show surface fault traces from the Southern California Earthquake Center Community Fault Model (CFM). Each black dot represents a site of interest covering a region within a 20 km radius. Inset shows cell boundaries and overlapping of the grid cells near the Salton Sea area. (b) Earthquake density, representing the average number of earthquakes per year that have magnitudes above the $M_c$ within each grid cell. (c) Magnitude of completeness attributed to the grids. Grids that have less than 500 earthquakes during the study period are excluded.

et al., 2019). This catalog has nearly 900 thousand earthquakes across southern California. We opt to use the 12 times MAD version (QTM-12) over the 9.5 times MAD QTM version (QTM-9.5) because it is more robust and is free from occasional day-long seismicity bursts that could be misinterpreted as triggering by our algorithm (e.g., Moutote et al., 2021).

We consider 1,580 global $M \geq 6$ earthquakes between 2008 and 2017, obtained from the International Seismological Centre (ISC) bulletin (International Seismological Centre, 2022) as possible candidate trigger earthquakes. We omit earthquakes from January to June 2008 and July to December 2017 to ensure sufficient data for the candidate earthquakes. We also do not consider global earthquakes that occurred in the two months after the 2010 El Mayor Cucapah Earthquake, the only $M \geq 6$ earthquake in the QTM catalog, due to its extended triggering behavior in southern California (e.g., Inbal et al., 2017; Meng & Peng, 2014). In total, 1,388 candidate earthquakes are investigated in this study.

To investigate local ground motions caused by the candidate trigger earthquakes, we examine the three-component, broadband, velocity seismograms recorded by stations in the region of interest, which roughly brackets southern California from 31° to 38° in latitude and from −123° to −113° in longitude. For each candidate event, we download data from 10 min before the candidate earthquake origin time to 2 hr after. Thus, the data contains a 10-min pre-event noise window and a 2-hr signal window, which includes body wave phases and minor arc surface wave phases.

## 2.2. Study Area

We focus on identifying dynamic triggering in southern California where the QTM catalog continuously reported local earthquakes (Figure 1). We gridded the region into 429 circular sites centered on well-documented surface fault traces from the Southern California Earthquake Center (SCEC) Community Fault Model (Marshall et al., 2022). Each site, or grid, has a radius of 20 km and is spaced about 20 km apart, with overlapping cells to avoid missing cases of dynamic triggering (inset, Figure 1a). The site area is termed a grid cell, and the site center is termed a grid node. Our gridding approach contains 99.3% of all catalog seismicity and is more efficient than a uniform gridding scheme. We only considered earthquakes with magnitudes greater than the magnitude of completeness ($M_c$) for each grid (Wiemer, 2000), and evaluated cells with at least 500 qualified earthquakes during the study period (Figure 1c). This approach led to 185 grid cells containing 98.7% of the QTM-12 seismicity.

## 2.3. Dynamic Triggering Identification

We hypothesize that statistically significant changes in seismicity-rates within the immediate 24 hr following a candidate earthquake are likely caused by earthquake dynamic triggering, although the exact mechanisms are

uncertain (e.g., Brodsky & van der Elst, 2014). Previous studies have reported delay times ranging from minutes to weeks (e.g., Gomberg et al., 2001; Hill, 2008; Hill & Prejean, 2015), and we follow the convention to focus on the first 24 hr after an earthquake (Hill & Prejean, 2015). The seismicity-rate and moment-release anomalies are examined using the $\beta$-, $Z$-, $\beta_m$-, and $Z_m$-statistics, as described in Sections 2.3.1 and 2.3.2.

The statistics compare seismicity or seismic moment within two different time periods, $\delta_a$ and $\delta_b$, where $\delta_a$ is the time period of interest and $\delta_b$ is the reference time period. We evaluate seismicity-rate and moment-release changes within 2-, 6-, 12-, and 24-hr time windows at each grid after the candidate earthquake origin time as the time period of interest ($\delta_a$). We use a 60-day reference time period ($\delta_b$) for the $\beta$- and $\beta_m$-statistics and a 30-day period before the candidate earthquake for the $Z$- and $Z_m$-statistics. The 2-hr window is used to monitor possible instantaneous triggering, and the other three windows are used to characterize delayed dynamic triggering. Positive values suggest an increase in seismicity-rate or moment-release, and negative values suggest a decrease. The instantaneous-triggering window length can be shorter, albeit at the cost of the robustness of the statistics due to the small number of samples. The time window length and reference period can be adjusted for customized applications.

### 2.3.1. $\beta$- and $\beta_m$-Statistics

The $\beta$-statistic characterizes seismicity-rate changes with respect to a reference time period that is normalized by its standard deviation (a dispersion parameter),

$$\beta = \frac{N_a - \bar{N}_a}{\sigma_a}, \tag{1}$$

where $N_a$ is the number of earthquakes during the time period of interest ($\delta_a$), and $\bar{N}_a$ and $\sigma_a$ are its expected value and standard deviation during the reference time period ($\delta_b$). The analytical solution of the expected value is $\bar{N}_a = \Lambda = N_b \cdot \frac{\delta_a}{\delta_b}$. For a Poissonian distribution, the standard deviation is $\sigma_a = \sqrt{\Lambda}$. Alternatively, $\bar{N}_a$ and $\sigma_a$ can be estimated empirically from the statistical population of $N_a$. Specifically, we randomly reposition the $\delta_a$ time window within the $\delta_b$ time window 10,000 times to obtain samples of $N_a$, leading to

$$\bar{N}_a = \frac{1}{M} \sum_{i=1}^{M} N_i, \tag{2}$$

$$\sigma_a = \sqrt{\frac{1}{M-1} \sum_{i=1}^{M} \left( N_i - \bar{N}_a \right)^2}, \tag{3}$$

where $M$ is the number of samples (10,000 in this study) and $N_i$ is the earthquake number in the $i$th reposition time window. The $\beta$-statistic of the original time period of interest is denoted as $\beta_0$. The procedure is similar to that outlined in Fan et al. (2021), but $\bar{N}_a$ and $\sigma_a$ are obtained empirically from the sampled population and our new procedure is free from earthquake occurrence assumptions. To compute the $\beta$-statistic, the $\delta_a$ and $\delta_b$ windows must include at least three and ten earthquakes, respectively. This quality-check criteria also applies when computing other statistics. The procedure is performed for every candidate trigger earthquake at every grid and time window with adequate seismicity.

Typically, the $\beta$-statistic is considered 95% significant when $\beta \geq 1.96$ (Wyss & Marsan, 2011). In this case, the $\beta$-statistic attends to a zero-mean, unit-variance Gaussian distribution, which is a result of the Poissonian assumption about seismicity occurrence (Wyss & Marsan, 2011). However, the assumption may be inaccurate and the $\beta \geq 1.96$ threshold may cause erroneous identifications of significant seismicity-rate changes (e.g., Fan et al., 2021; Marsan & Nalbant, 2005; Pankow & Kilb, 2020; Prejean & Hill, 2018). Therefore, we adopt the sampling procedure described in (Fan et al., 2021) to evaluate the statistical significance of $\beta_0$ at the 95% confidence level. We consider the seismicity-rate change statistically significant for the given time window $\delta_a$ and grid if $\beta_0 > \beta_{95\%}^a$ and $\beta_0 > \beta_b$ (e.g., Figure 2c and Fan et al., 2021). $\beta_{95\%}^a$ is a 95th percentile threshold calculated from the previously obtained $N_a$ samples, and $\beta_b$ is calculated for local seismicity immediately preceding the candidate trigger. Additional details can be found in Fan et al. (2021) and Text S1 in Supporting Information S1. For such cases, we hypothesize that the seismicity-rate change was caused by dynamic triggering.

When computing the $\beta$-statistic for seismicity-rate changes, earthquakes with different magnitudes are treated equally as only their occurrences are evaluated. Here we develop a new moment-release statistic, the $\beta_m$-statistic, to
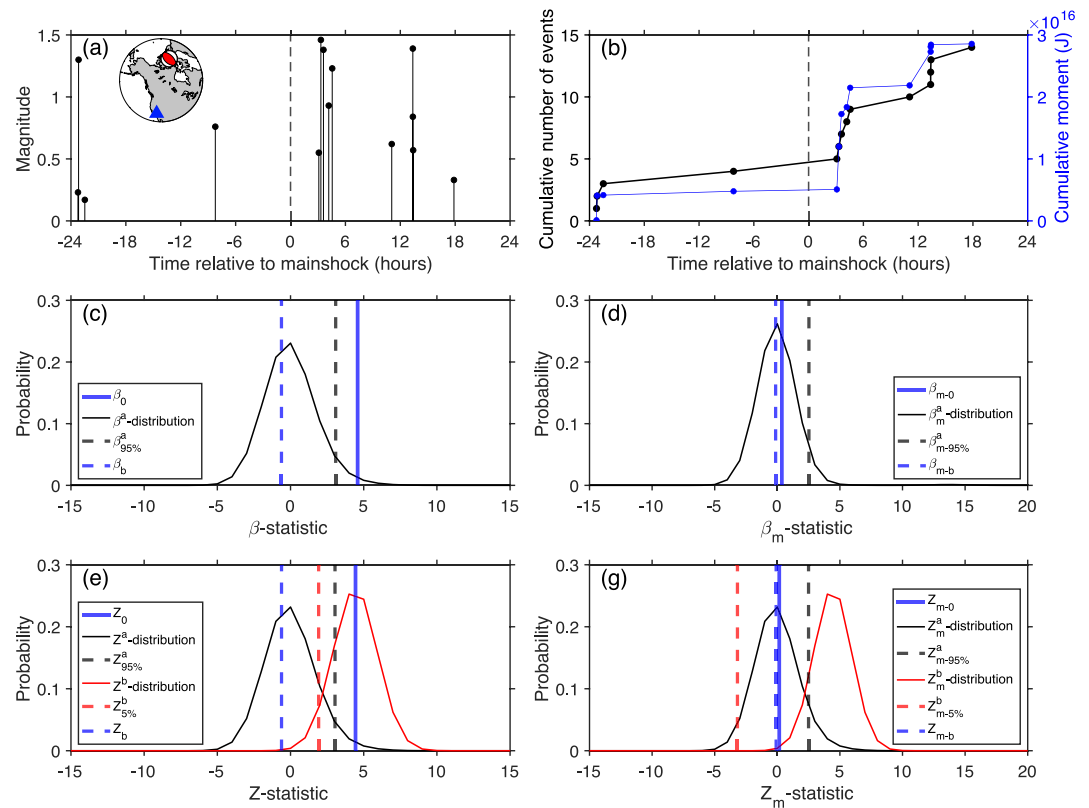
**Figure 2.** Example statistic distributions at a grid near the Coso Geothermal Field for $\delta_a$ as 6 hr. (a) Earthquake occurrence within 24 hr of the candidate trigger earthquake. Three and ten earthquakes occurred before and after the candidate earthquake, respectively. Inset: candidate trigger earthquake (2017-01-08 23:47:13.66, M6.0, ISC ID: 611831502) and the study site. (b) Cumulative seismicity and moment-release within 24 hr of the candidate trigger earthquake. (c) $\beta$-statistic distribution ($\beta^a$-distribution), $\beta_0$, and the associated thresholds $\beta_b$ and $\beta^a_{95\%}$. (d) $\beta_m$-statistic distribution ($\beta^a_m$-distribution), $\beta_{m-0}$, and the associated thresholds $\beta_{m-b}$ and $\beta^a_{m-95\%}$. (e) Z-statistic distributions ($Z^a$- and $Z^b$-distributions), $Z_0$, and the associated thresholds $Z_b$, $Z^a_{95\%}$, $Z^b_{5\%}$. (f) $Z_m$-statistic distributions ($Z^a_m$- and $Z^b_m$-distributions), $Z_{m-0}$, and the associated thresholds $Z_{m-b}$, $Z^a_{m-95\%}$, $Z^b_{m-5\%}$.

identify region-specific anomalies which can reveal when and where larger-than-expected earthquakes were triggered. To calculate $\beta_m$, we compare the seismic moment of earthquakes in $\delta_a$ to the seismic moment-release in the reference time period $\delta_b$. For simplicity, we use the magnitudes ($m$) from the QTM catalog as moment-magnitudes, even though this estimate may be biased (e.g., Shearer et al., 2022). However, the statistic focuses on relative differences so the identification of moment-release anomalies is not affected. The seismic moment-release in $\delta_a$ is described by $\bar{M}_a$ and $\sigma_{M_a}$, and $\beta_m$ is formulated as

$$\beta_m = \frac{M_a - \bar{M}_a}{\sigma_{M_a}}, \tag{4}$$

where

$$M_a = \sum_{i=1}^{N_a} 10^{1.5m_i + 9.1}. \tag{5}$$

The significance of the $\beta_m$-statistic is evaluated similarly to $\beta$; the moment-release change is statistically significant for a given time window $\delta_a$ at a grid when $\beta_{m-0} > \beta^a_{m-95\%}$ and $\beta_{m-0} > \beta_{m-b}$ (e.g., Figure 2d).

### 2.3.2. Z- and $Z_m$-Statistics

The Z-statistic is a symmetric measure of the seismicity-rate changes, which significance depends on seismicity in both the time period of interest and reference window (Wyss & Marsan, 2011). Following Habermann (1983), we compute the Z-statistic as

$$Z = \frac{N_a/\delta_a - N_b/\delta_b}{\sqrt{(\sigma_a/\delta_a)^2 + (\sigma_b/\delta_b)^2}}, \tag{6}$$

where $N_b$ is the number of earthquakes within $\delta_b$, $\sigma_b$ is the standard deviation associated with the distribution of $N_b$, and $N_a$, $\delta_a$, $\delta_b$, and $\sigma_a$ are defined as above. The $Z$-statistic results are compared with those of the $\beta$-statistic for the same earthquakes.

The $Z$-statistic is free from seismicity occurrence assumptions if $\sigma_a$ and $\sigma_b$ are estimated empirically. In addition to sampling $N_a$ as before, we also sample the $N_b$ population by randomly repositioning the $\delta_b$ window 10,000 times within 1 year of the candidate trigger earthquake, ranging from six months before to 6 months after the event origin time. We estimate the population statistics for the $N_b$ population, particularly the expected value and standard deviation ($\sigma_b$), which are then used to compute a $Z$-statistic for the candidate trigger earthquake at a given grid. We note that the sampling procedure implicitly assumes that $\sigma_a$ and $\sigma_b$ are invariant throughout their respective sampling time periods, which is 30 days for $\sigma_a$ and 1 year for $\sigma_b$. For a given case, if the $Z$-statistic exceeds $Z_{95\%}^a$, $Z_b$, and $Z_{5\%}^b$ (e.g., Figure 2e), we consider the seismicity-rate change anomalous. $Z_{95\%}^a$ and $Z_b$ are thresholds representing the 95th percentile and preceding window, similar to those of the $\beta$-statistic, and $Z_{5\%}^b$ is a 5th percentile threshold obtained from sampling $N_b$ (Fan et al., 2021 and Text S1 in Supporting Information S1).

Similar to the $\beta_m$-statistic, we design the $Z_m$-statistic to detect seismic moment-release anomalies. The $Z_m$-statistic is given by:

$$Z_m = \frac{M_a/\delta_a - M_b/\delta_b}{\sqrt{(\sigma_{Ma}/\delta_a)^2 + (\sigma_{Mb}/\delta_b)^2}}, \tag{7}$$

where $M_b$ follows Equation 5 but for the $\delta_b$ time period. There is a significant anomaly when $Z_{m-0} > Z_{m-95\%}^a$, $Z_{m-0} > Z_{m-b}$, and $Z_{m-0} > Z_{m-5\%}^b$ (e.g., Figure 2g).

Taking the 8 January 2017 M6 Queen Charlotte earthquake as an example trigger earthquake (Figure 2a), we find that the earthquake may have triggered seismicity at the Coso Geothermal Field within 6 hr of its origin time (Figure 2 and Table S1 in Supporting Information S1), which is supported by both the $\beta$-statistic and $Z$-statistic. However, neither the $\beta_m$- or $Z_m$-statistic suggests anomalous moment-release change at the location during the 6-hr time window.

Our study extends the work of Fan et al. (2021) in several aspects. We propose new statistics to investigate moment-release anomalies and compare with the $Z$-statistic. Unlike Fan et al. (2021), we obtain the expected values and standard deviations from sampling rather than analytical solutions, simplifying the procedure by removing the $\beta_{5\%}^b$ threshold used in Fan et al. (2021). We also use different earthquake catalogs: the ISC bulletin for global events (International Seismological Centre, 2022) and the QTM-12 version for local earthquakes (Ross, Trugman, et al., 2019). Moreover, we investigate all available regions in southern California using a gridding scheme guided by the SCEC Community Fault Model (Marshall et al., 2022). Lastly, we designed a comprehensive set of tests to evaluate the algorithm performance and associated uncertainties.

### 2.4. Waveform Metrics

We analyze velocity waveforms of candidate trigger earthquakes in southern California and measure four instantaneous waveform metrics: peak ground velocity, peak frequency, kinetic energy, and relative frequency content. The peak ground velocity (PGV) is measured in two frequency bands (0.01–0.1 Hz and 1–5 Hz; Figures 3a and 3b). The 0.1–1 Hz frequency band is not investigated here due to high noise levels from microseisms. We remove the instrument response, decimate the data to 20 Hz for computational efficiency, bandpass filter the records, and compute their envelope functions. The maximum envelope amplitudes are then measured in both the pre-event noise window (10 min) and the signal window (two hours) independently for all three channels at each station. We compute a signal-to-noise ratio (SNR) as the ratio between the maximum amplitudes of the signal and noise windows for each channel and only use traces with SNR greater than 5 in both the low- and high-frequency bands for all three channels to measure the four waveform metrics. We take the geometric mean of the qualified waveform envelopes and calculate a single PGV value for the station, and use the same qualified traces for calculating the other metrics. Figures 3a and 3b demonstrates an example of
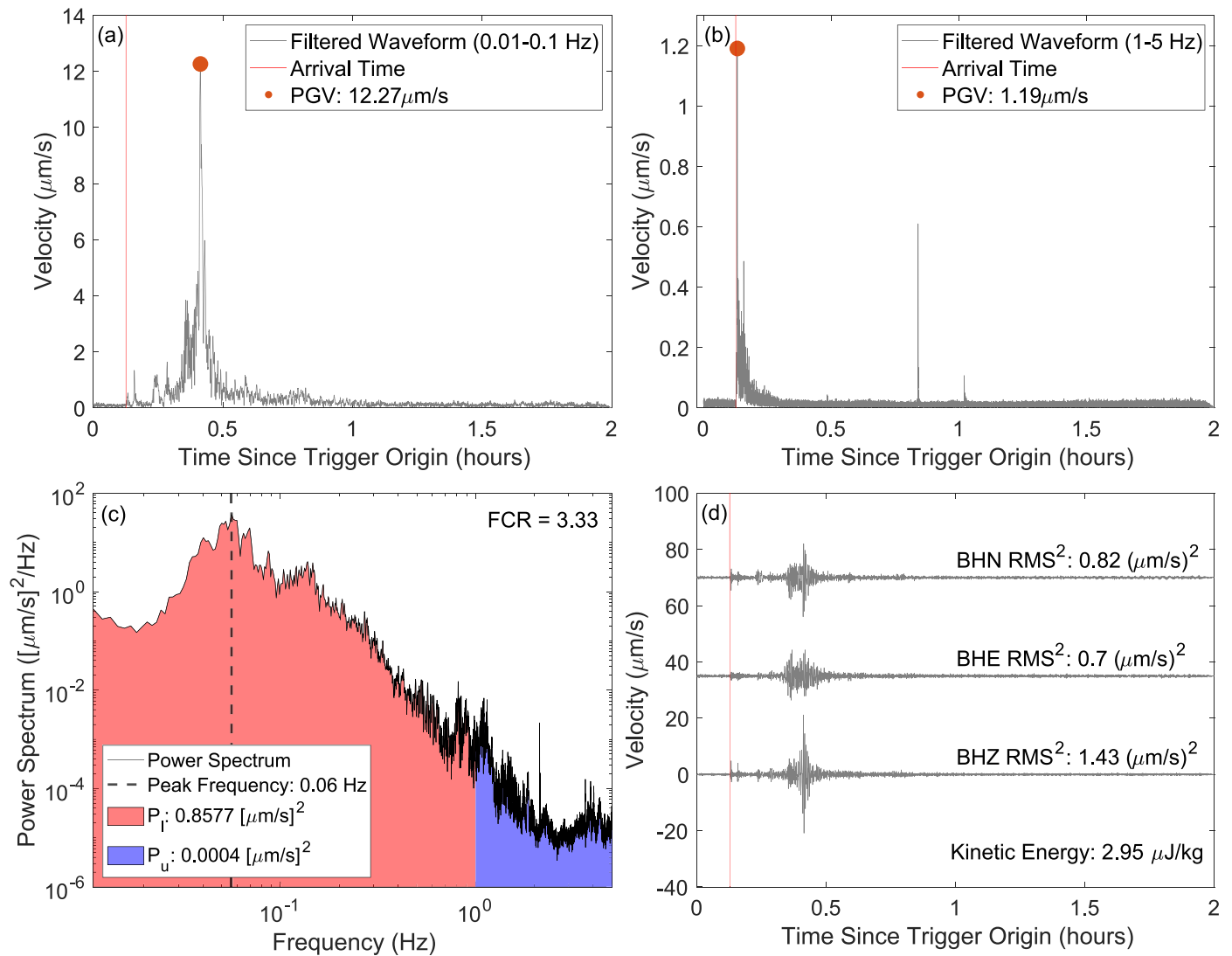
**Figure 3.** Waveform metric calculations of the 8 January 2017 M6 Queen Charlotte earthquake at station CI.JRC2, near the Coso Geothermal Field. The P-wave arrival time is calculated using the Preliminary Earth Reference Model (Dziewonski & Anderson, 1981). (a–b) Waveform envelopes (geometric mean of the three-component envelopes) at the 0.01–0.1 Hz and 1–5 Hz frequency bands. The maximum amplitudes of the envelopes are taken as the PGV of the frequency bands, respectively. (c) Geometric mean of the three-component power spectra. Peak frequency corresponds to the frequency yielding the maximum value of the spectrum. FCR is calculated using the integral results $P_l$ in the 0.01–1 Hz band and $P_h$ in the 1–5 Hz band (Equation 9). (d) Band-pass filtered waveforms (0.01–10 Hz). Square sum of the three-component RMS values is taken as the kinetic energy per unit mass. The BHE and BHN data are shifted 35 and 70 µm/s upwards, respectively, for visual clarity.

measuring the PGV values of the 2017 M6 earthquake in the Queen Charlotte Islands, Canada at CI.JRC2 (near Coso) in the two frequency bands. The PGV values in the upper frequency band may be influenced by local seismicity.

We estimate the peak frequency of ground velocity records at each station for the candidate trigger earthquakes (e.g., Figure 3c). We use the multitaper method with 11 Slepian tapers to estimate the power spectrum of the waveform in the signal window for each channel (Thomson, 1982). Given almost all candidate earthquakes are at teleseismic distances, we focus on the 0.01–5 Hz frequency band and compute the geometric mean of the power spectra from the three channels. The corresponding frequency of the maximum power is taken as the peak frequency.

To calculate kinetic energy, we band-pass filter the data at 0.01–10 Hz (Figure 3d) and compute the root-mean-square (RMS) values for each channel in the signal window, resulting in three measurements per station. We then record the square-sum of the RMS measurements as the kinetic energy per unit mass for the
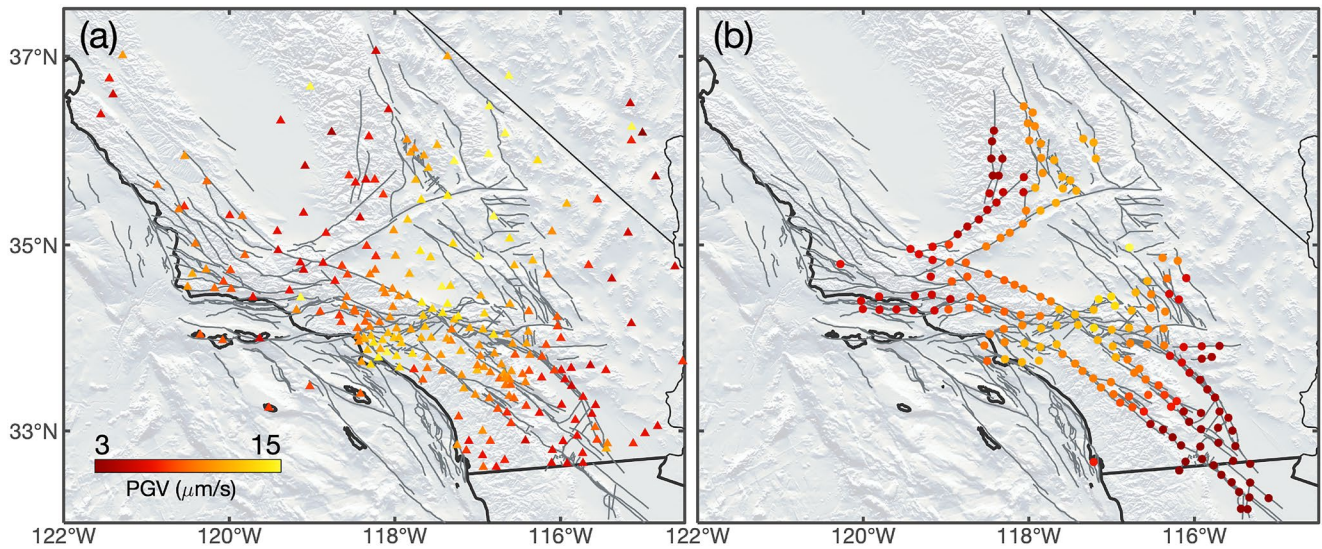
**Figure 4.** Example station-grid interpolation of PGV values in the 0.01–0.1 Hz band for the 8 January 2017 M6 Queen Charlotte earthquake. (a) Measured values at each station. (b) Interpolated values at qualified grid points.

earthquake-station pair. Figure 3d shows an example of measuring the kinetic energy for the M6 Queen Charlotte earthquake at CI.JRC2.

Lastly, we examine the relative frequency content of the passing waveforms. We modify the Frequency Index (FI) metric (Buurman & West, 2010) given by:

$$FI = \log_{10}\left(\frac{\bar{A}_u}{\bar{A}_l}\right), \tag{8}$$

where $\bar{A}_l$ is the mean power spectrum amplitude in a lower frequency band and $\bar{A}_u$ in an upper frequency band. We use the integrated total power within each frequency band instead of the mean spectral amplitudes for a more stable calculation. This metric is referred to as the Frequency Content Ratio (FCR):

$$FCR = \log_{10}\left(\frac{\int_{f_{l1}}^{f_{l2}} S(f)\,df}{\int_{f_{u1}}^{f_{u2}} S(f)\,df}\right) = \log_{10}\left(\frac{P_l}{P_u}\right) \tag{9}$$

where $S(f)$ is the geometric mean of the power spectra of the three channels, and $f_{l1}, f_{l2}, f_{u1}, f_{u2}$ define the lower and upper frequency bands. Here the lower frequency band is taken as 0.01–1 Hz, and the upper frequency band is 1–5 Hz (Figure 3c). We place the lower band in the numerator to ensure that the FCR estimates are primarily positive for teleseismic earthquakes, due to their more prominent low frequency signals.

The waveform metrics are computed for each station independently, and the measurements for each candidate trigger earthquake at a given grid are interpolated from nearby stations. For each grid, the waveform metric measurements are taken as the median values of the metrics at the three to five closest stations (Figure 4). The stations are required to be within 100 km from the grid node, and at least three stations are required to obtain a valid measurement. Otherwise, the measurement value is not considered for the grid.

## 3. Results

In this section, we detail our observations of seismicity and moment-release anomalies in southern California associated with the candidate earthquakes, focusing on their spatial (Section 3.1) and temporal (Section 3.2) patterns. We focus on general patterns since exact uncertainties are challenging to propagate for the collection of cases and stem from a subjective decision on the significance level. Since the seismicity-rate anomalies are identified at a 95% confidence level, we omit grid points that were triggered less than 5 times from our results

**Table 1**
*Summary of Dynamic Triggering Results in Southern California*

|  | $\beta$ | $Z$ | $\beta_m$ | $Z_m$ |
|---|---|---|---|---|
| Percent of grids triggered (185 total grids) | 64% | 50% | 54% | 40% |
| Percent of candidates that trigger (1,388 total) | 70% | 60% | 52% | 32% |
| Percent of triggering cases that are delayed | 83% | 79% | 91% | 89% |
| Percent of instantaneous cases that are extended | 51% | 46% | 63% | 59% |

and discussion (see Section 4.1 for details). In general, we find that up to 70% of candidate trigger earthquakes may have caused dynamic triggering in southern California from 2008 to 2017. We find that triggering occurrence varies from fault to fault, and triggering occurs most often at the Salton Sea and Coso geothermal fields as well as the San Jacinto fault. Furthermore, we identify temporal patterns evolving at multiple scales, from instantaneous to delayed responses, and from intermittent occurrence at a given grid to frequent triggering in southern California. Lastly, we examine the waveform metrics of candidate trigger earthquakes at grids with both normal and anomalous seismicity-rate and moment-release changes.

### 3.1. Spatial Triggering Patterns

Dynamic triggering is likely widespread in southern California (Table 1), and we have identified dynamic triggering of seismicity with more than five occurrences at about half of the considered grids. Anomalous seismic moment-release is less commonly observed in comparison, but has been observed at over 40% of the grids. The spatial patterns of triggering occurrence for the four test statistics exhibit high heterogeneity as shown by the triggering occurrence distributions (Figure 5), which count the number of candidate trigger earthquakes that caused seismicity or moment-release anomalies in any of the four time windows ($\delta_a$ as 2, 6, 12, or 24 hr). The Salton Sea Geothermal Field (SSGF), Coso Geothermal Field (CGF), and San Jacinto fault (SJF) most frequently experienced seismicity-rate anomalies (Figures 5a and 5c). Remote earthquakes also frequently trigger seismicity at the Elsinore fault, the intersection of the San Andreas and San Jacinto faults, the southern San Andreas fault, the southern Sierra Nevada, and the Ridgecrest region. In contrast, moment-release anomalies have different spatial patterns than those of the seismicity-rate anomalies (Figures 5b and 5d), with the SSGF and CGF less likely to have moment-release anomalies than SJF, and their triggering occurrence is comparable to that of the Elsinore fault. Moment-release anomalies are less frequently observed at the intersection of the San Andreas and San Jacinto faults, Ridgecrest area, and southern San Andreas fault (Figures 5b and 5d).

We observe delayed triggering cases (6–24 hr windows, Figure 6 and Figure S1 in Supporting Information S1) more frequently than instantaneous cases (2 hr, Figure 6) for all four statistics. Our findings suggest that delayed dynamic triggering of both seismicity and moment-release is a common occurrence in southern California at multiple grids. Although instantaneous triggering cases are challenging to observe due to the passing wave coda, our results show that nearly all cases of moment-release anomalies are delayed (Table 1). Around half of instantaneously triggered cases of seismicity or moment-release also extended into later hours (Table 1).

Our results confirm the triggerability pattern reported by Miyazawa et al. (2021) for most locations in southern California, with some differences at the Beta Offshore Platform, San Andreas fault, and the southern Sierra. In their study, Miyazawa et al. (2021) used the QTM-9.5 catalog and inverted for triggerability based on distributions of separation times between the candidate earthquake and the local earthquakes immediately preceding and following the candidate, whereas we examine seismicity in the entire time window. Our results are consistent with the global ubiquity of dynamic triggering reported by Velasco et al. (2008), who found an 80% triggering rate for $M \geq 7$ candidates.

### 3.2. Temporal Triggering Patterns

To investigate the temporal evolution of dynamic triggering processes, we examine the local recurrence times, defined as the time intervals between consecutive triggering events at each grid. We also analyze the interevent time, which is the time interval between consecutive triggering events for any grid in southern California.

The spatial pattern of recurrence times correlates with triggering occurrence, with strong heterogeneity from grid to grid (Figures 5 and 7). Median recurrence times range from tens of days to years for different grids, with adjacent grids exhibiting similar recurrence times. For example, the SSGF, CGF, and SJF frequently experience seismicity-rate anomalies, with average recurrence times of approximately 2–2.5 months (Figure 7). In contrast, the Los Angeles basin exhibits infrequent seismicity-rate anomalies, with gaps of several years between triggering cases. Similarly, moment-release anomalies are infrequent in the geothermal fields, consistent with the spatial pattern observed in Figure 5. For example, Figures 8a–8d shows the distributions of recurrence times for
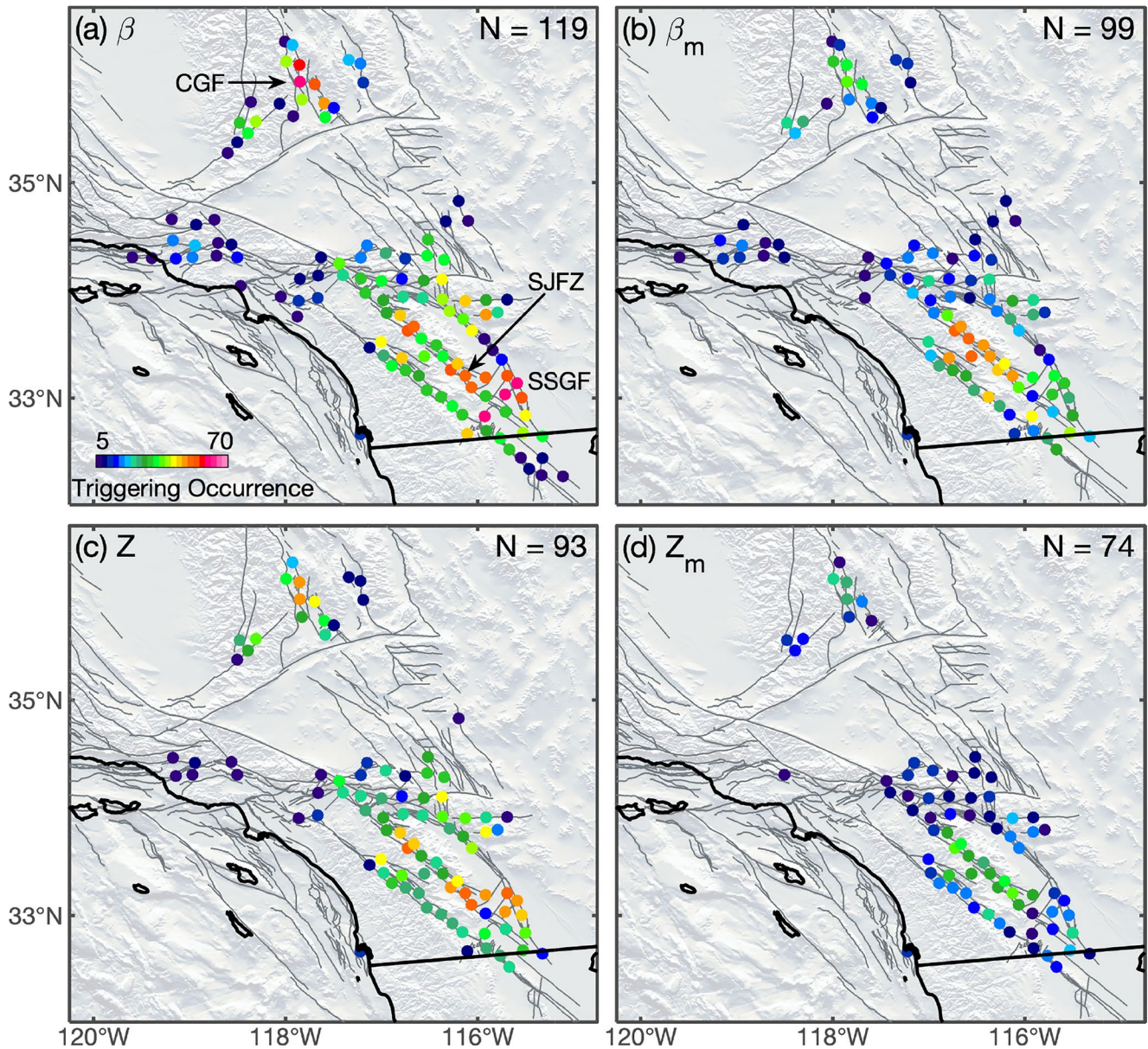
**Figure 5.** Spatial triggering patterns in southern California. Triggering occurrences identified using the $\beta$-statistic (a), $\beta_m$-statistic (b), $Z$-statistic (c), and $Z_m$-statistic (d) are denoted in color. Triggering occurrence is the number of candidate trigger earthquakes that caused seismicity or moment-release anomalies in any of the four time windows. $N$ denotes the number of triggered grids. Salton Sea Geothermal Field (SSGF), San Jacinto Fault Zone (SJFZ), and the Coso Geothermal Field (CGF) are prone to triggering.

a few notable locations using the $\beta$-statistic. Similar figures for other statistics are provided in Supporting Information S1 (Figures S2–S4).

On average, dynamic triggering of seismicity is observed every 3.4 and 3.9 days using the $\beta$- and $Z$-statistics, respectively, at one or more of the grids in southern California. Similarly, moment-release anomalies from the $\beta_m$- and $Z_m$-statistics occur every 4.5 and 7.4 days on average in the region. The distributions of interevent times in southern California are summarized in Figures 8e–8h, indicating that dynamic triggering occurs frequently in southern California on a scale of every few days. We also explored temporal variations of the recurrence and interevent times in the region during the study period, such as changes in the triggering patterns due to the 2010 El Mayor Cucapah earthquake and the 2019 Ridgecrest earthquakes. However, we do not identify significant variations in the triggering patterns using the QTM-12 catalog.
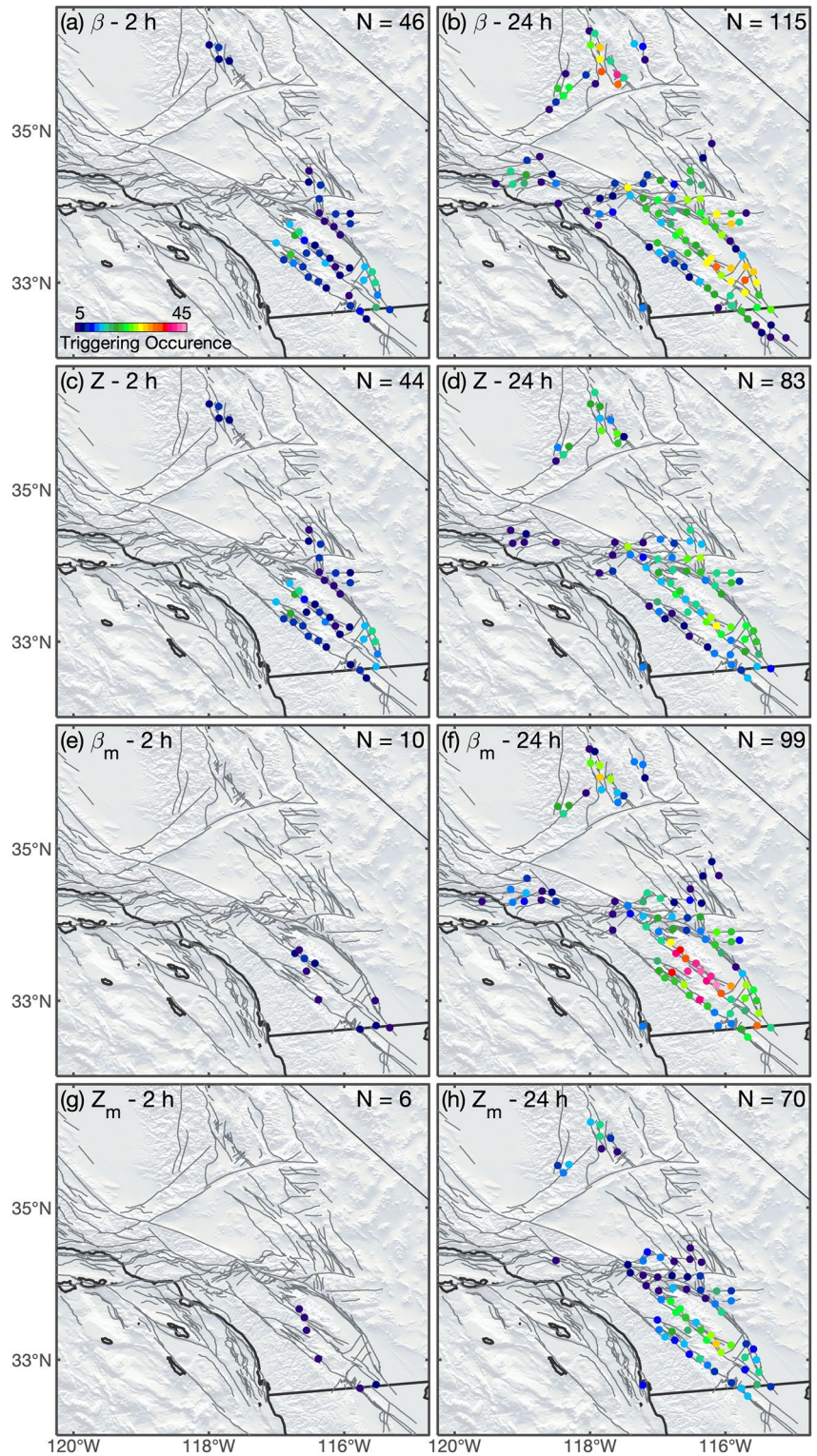
**Figure 6.** Triggering occurrences during the 2 and 24 hr ($\delta_a$ as 2 and 24) time windows using the $\beta$-statistic (a, b), $Z$-statistic (c, d), $\beta_m$-statistic (e, f), and $Z_m$-statistic (g, h). $N$ denotes the number of triggered grids.
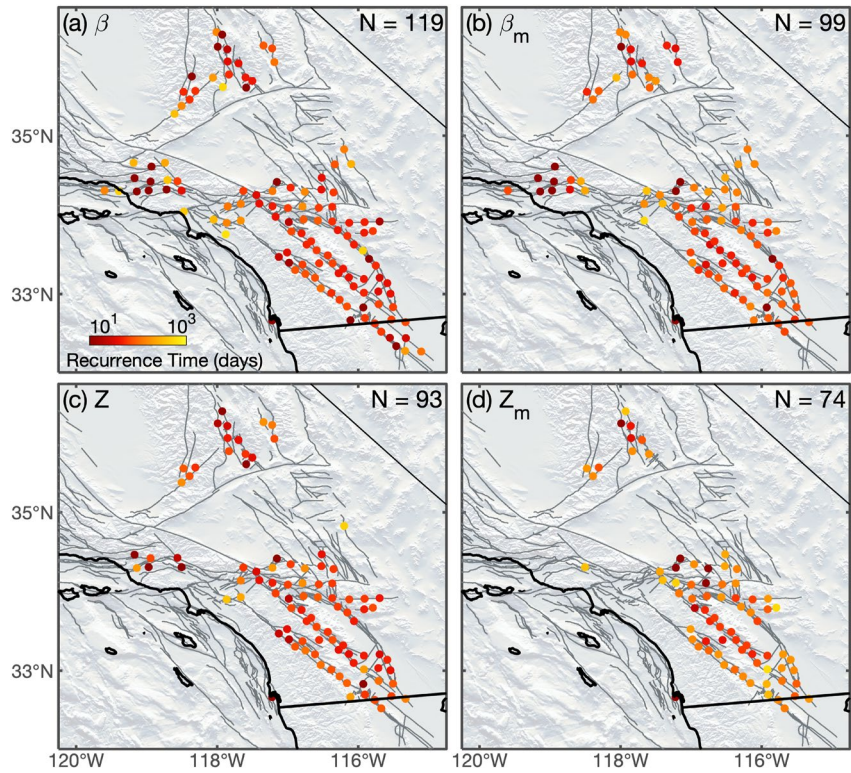
**Figure 7.** Median recurrence times at the qualified grids using the $\beta$-statistic (a), $\beta_m$-statistic (b), $Z$-statistic (c), and $Z_m$-statistic (d). $N$ denotes the number of triggered grids.
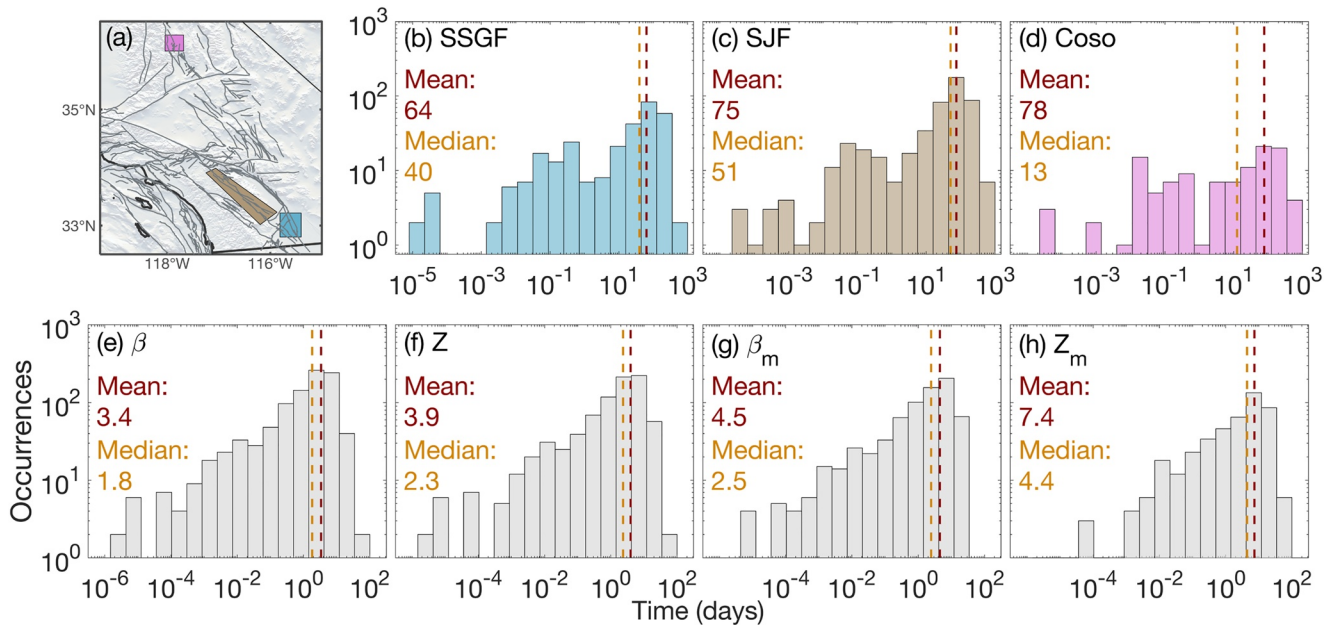


**Figure 8.** Distribution of triggering recurrence times at example locations and distributions of interevent times (in days) for southern California. (a) Map view of three locations. Polygons may include more than one grid node, for example, the San Jacinto fault Zone. (b–d) Recurrence times at the Salton Sea Geothermal Field (b), the San Jacinto fault Zone (c), and the Coso Geothermal Field (d). (e–f) Interevent times for southern California obtained using the $\beta$-statistic (e), $Z$-statistic (f), $\beta_m$-statistic (g), and $Z_m$-statistic (h).
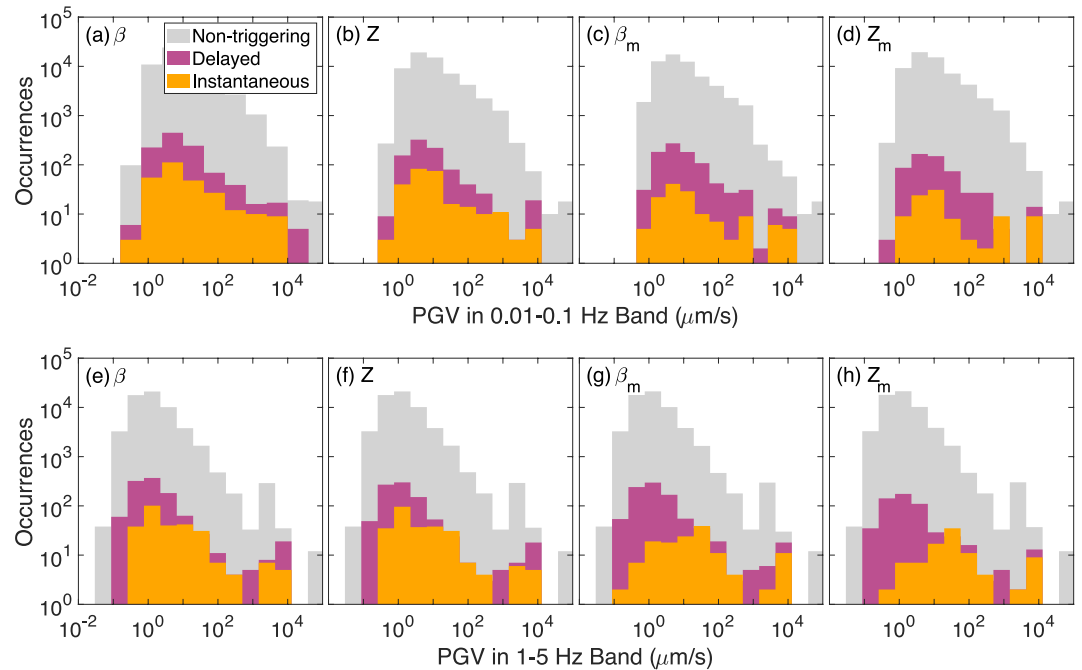
**Figure 9.** Distributions of PGV values in the 0.01–0.1 Hz (a–d) and 1–5 Hz (e–h) frequency bands for triggering cases identified using the $\beta$-statistic (a, e), $Z$-statistic (b, f), $\beta_m$-statistic (c, g), and $Z_m$-statistic (d, h). Histograms are color coded to represent the instantaneous triggering (orange), delayed triggering (plum), and non-triggering cases (gray).

### 3.3. Waveform Results

We have analyzed waveform metrics for the 1,388 candidate trigger earthquakes for grids that have been triggered at least five times, as shown in Figures 3 and 4. The waveform metrics at grids that have not been triggered show similar values (Figure S22 in Supporting Information S1). The waveform metrics can have significant variations across the study area (Figure 4 and Figure S24 in Supporting Information S1), and triggering and non-triggering sites exhibit similar variability. For comparison, the measurements are then grouped into three categories: instantaneous (2-hr window), delayed (6- to 24-hr windows), and non-triggering. We find no significant differences between the three groups for PGV distributions in the 0.01–0.1 Hz band (Figures 9a–9d). However, instantaneous triggering cases have a larger minimum PGV than delayed cases in the 1–5 Hz band (Figures 9e–9h). On average, a PGV threshold of 0.2 and 0.5 μm/s in the 1–5 Hz band seems to be observed for the instantaneously triggered seismicity and moment-release anomalies, respectively. However, the threshold does not exclude occurrence of delayed and non-triggering cases as there are incidences of both groups with similar or greater PGV values. The observed high-frequency threshold is also observed in the FCR metric, manifesting as a leftward shift of the instantaneous distributions (Figures 10e–10h). There are no obvious differences in the distributions of the peak frequency or kinetic energy for the four test statistics (Figure 10). The waveform characteristics could not deterministically differentiate the triggering incidences from non-triggering cases or separate instantaneous and delayed cases. However, the fraction of identified triggering cases seems to increase with PGV values (Figure S23 in Supporting Information S1). For example, about 35% and 45% of grids with measured 1–5 Hz PGV values greater than 4,000 μm/s associate with dynamic triggering cases identified by the $\beta$- and $\beta_m$-statistics, respectively (Figure S23 in Supporting Information S1).

## 4. Discussion

Dynamic triggering occurs ubiquitously in southern California, albeit with strong occurrence heterogeneity in space and time. In this section we will first evaluate the identification uncertainty and limitation (Sections 4.1 and 4.2), and then examine possible triggering mechanisms (Section 4.6).

### 4.1. Uncertainty

In this study, we identify seismicity-rate and moment-release anomalies at a 95% confidence level and associate them with candidate trigger earthquakes. We only consider grids with at least five triggering cases to ensure the
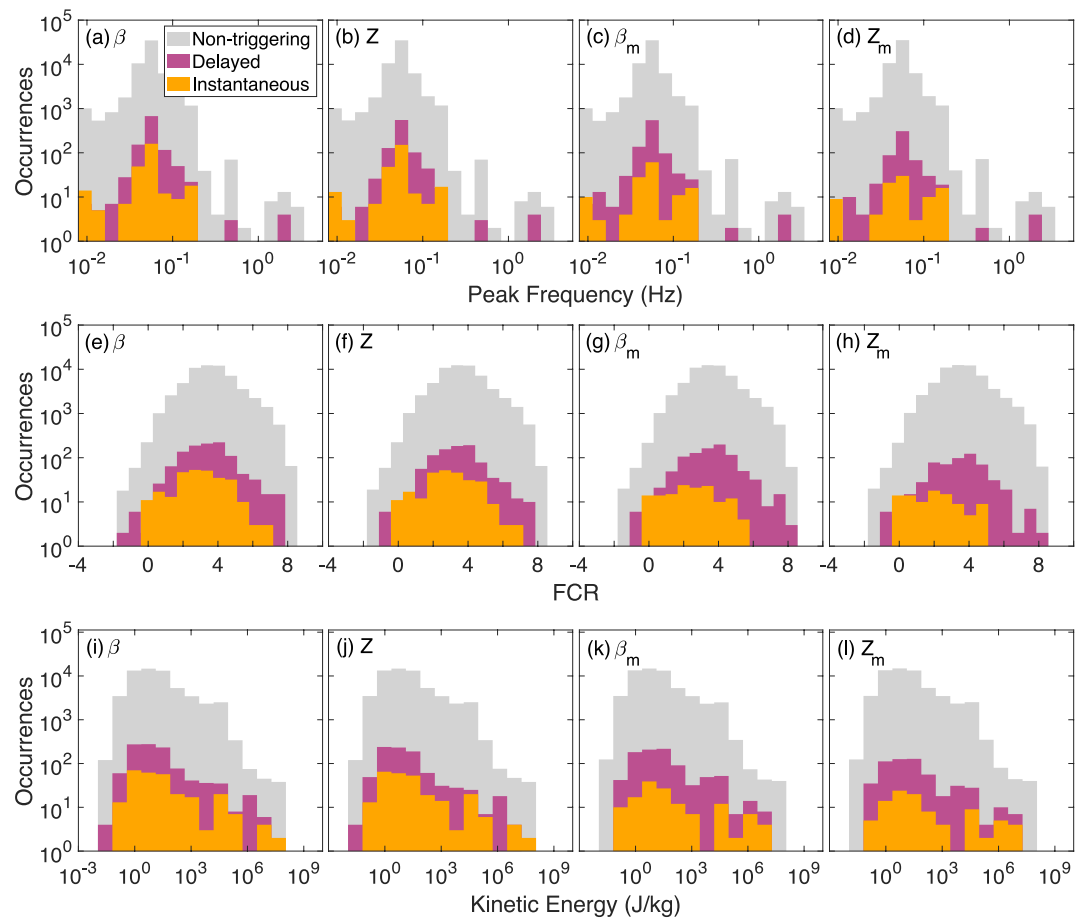
**Figure 10.** Distributions of peak frequency (a–d), FCR (e–h), and kinetic energy values for triggering cases identified using the $\beta$-statistic (a, e, i), $Z$-statistic (b, f, j), $\beta_m$-statistic (c, g, k), and $Z_m$-statistic (d, h, l). Histograms are color coded to represent the instantaneous triggering (orange), delayed triggering (plum), and non-triggering cases (gray).

robustness of the observed spatial patterns. The observed temporal patterns are better resolved for grids with frequent triggering cases, such as the SJF, the SSGF, and the CGF. Details on the five-times selection criterion are discussed in Supporting Information S1 (Text S2). Our uncertainty analysis confirms the robustness of the results and assesses potential biases introduced by various factors such as background seismicity, magnitude of completeness, window length, aftershocks, and consecutive candidate earthquakes with short separations.

We performed three tests to evaluate the robustness of our statistical procedures for identifying seismicity-rate and moment-release anomalies. These tests included generating two synthetic catalogs without triggering cases and one "synthetic" catalog by shuffling the QTM and ISC catalogs (see Tables S3–S5 in Supporting Information S1 for parameter details). We note that our tests focus on evaluating false positive cases, as our aim is to identify possible mechanisms that could cause dynamic triggering in southern California. We do not attempt to investigate the negatives.

We first generate a ten-year-long Poissonian catalog, where the occurrence of seismicity follows a Poisson distribution with magnitudes drawn from the Gutenberg-Richter Law (Fiedler et al., 2018; Gutenberg & Richter, 1944). Without losing generality, we assume that the seismicity occurs within one grid cell. We then randomly select 1,500 times to represent global candidate earthquakes, remove those which fall between January–June 2008 or July–December 2017, and apply the same statistical procedures as detailed in Section 2.3 to evaluate the seismicity-rate and moment-release significance. We calculated false positive rates by dividing the number of triggering identifications by the number of trials. The number of trials is the product of numbers of candidates, time windows, and grids. Results are shown in Table 2, and the false positive rates are below the 5% threshold (95% confidence level). We omitted scenarios where there was inadequate seismicity as applied to real data.

**Table 2**
*False Positive Rates of the Statistical Identification Procedures When Applied to the Poissonian, ETAS, and Shifted Catalogs*

| False positive rate | Poissonian catalog | ETAS catalog | Shifted catalog |
|---|---|---|---|
| $\beta$-statistic | 0.31% (5496) | 0.45% (5494) | 4.53% (142848) |
| $Z$-statistic | 0.31% (5496) | 0.44% (5494) | 3.63% (142493) |
| $\beta_m$-statistic | 2.27% (5496) | 0.96% (5494) | 3.89% (142848) |
| $Z_m$-statistic | 1.55% (5496) | 0.55% (5494) | 2.26% (142493) |

*Note.* The number of trials is indicated in parentheses. The rates are computed excluding trials without adequate seismicity (Section 2.3.1). All values are below the assumed false positive rate of 5% (95% confidence level).

To account for mainshock-aftershock sequences of local earthquakes that are not present in the Poissonian catalog, we generated a second synthetic catalog following the temporal Epidemic-Type Aftershock Sequence (ETAS) model (Ogata, 1988; Shearer, 2012a, 2012b). The ETAS catalog includes both random background seismicity and mainshock-aftershock sequences governed by the Omori-Utsu Law (Utsu, 1961). This test is designed to determine the false positive rates due to local mainshock-aftershock sequences (Table 2). We obtain false positive rates below the 5% threshold for all four statistics. These synthetic tests show that our procedure can distinguish dynamic triggering from random background seismicity and mainshock-aftershock sequences.

To further validate the robustness of our results, an alternative approach is to randomly shift the QTM and ISC $M \geq 6$ catalogs by a time delay between a week to 1 year, respectively, which is long enough to eliminate any potential correlations between the catalogs. By doing so, we can preserve the spatiotemporal clustering of the original catalogs while eliminating the possibility of dynamic triggering. We apply the same statistical procedures as detailed in Section 2.3 to the shifted catalogs and evaluate the significance of any identified seismicity-rate and moment-release anomalies. This approach provides an additional level of confirmation that our results are not influenced by spurious correlations or artifacts in the original catalogs. To expedite computation, we perform this test on eight grids that exhibit varying triggering responses (Table S5 in Supporting Information S1). Table 2 displays the results, which are all below 5%. These tests validate the efficacy of our method and confirm that the results are not biased by local earthquake clusters.

The aforementioned tests validate our method in identifying dynamic triggering due to far-field earthquakes. However, near-field dynamic triggering can also trigger local earthquakes (e.g., Felzer & Brodsky, 2006; Kilb et al., 2000; van der Elst & Brodsky, 2010). For example, the 2010 El Mayor Cucapah earthquake, the only $M > 6$ earthquake in the region during the study period, caused widespread near-field dynamic triggering in southern California (Meng & Peng, 2014; Ross, Trugman, et al., 2019). Near-field triggering is a complex process that may involve static triggering, frequency dependent dynamic triggering, or a concentration of aftershock nucleation sites near the mainshock (van der Elst & Brodsky, 2010). While these processes are all important, it is challenging to isolate their effects individually. Therefore, we chose to focus on remote events with large magnitudes that may cause a significant perturbation at the local fault system during the passing wave.

We have also tested if triggering occurrence correlates with the total number of earthquakes greater than $M_c$ within each grid cell (Figure 11a). The $\beta$- and $Z$-statistics show moderate correlation with earthquake number, with higher correlation for instantaneous triggering than delayed cases. Interestingly, we find a strong correlation between the triggering occurrence of moment-release anomalies and earthquake numbers, differing from the seismicity-rate patterns. These results differ from Miyazawa et al. (2021) but are in qualitative agreement with van der Elst and Brodsky (2010). These correlation coefficients suggest that areas with higher background seismicity-rates are moderately more likely to experience frequent dynamic triggering.

Dynamically triggered earthquakes are typically small (Hill & Prejean, 2015), and lower magnitudes of completeness permit the identification of more triggered cases (Li et al., 2022). We have tested the possibility by using the QTM-9.5 catalog, which has a lower $M_c$ than the QTM-12 catalog. This resulted in more triggering identifications but did not alter the overall triggering patterns or interpretations. Further increasing $M_c$ would likely lead to identifying fewer triggering cases with less reliable results. To ascertain the effect of varying $M_c$ on our observed spatial triggering patterns, we compute correlation coefficients between spatial patterns of the triggering occurrence and magnitude of completeness, which show no significant correlation for any test statistic (Figure 11b). The $\beta$- and $\beta_m$-statistics have a higher negative correlation with $M_c$ than the $Z$- and $Z_m$-statistics (Figure 11b). Overall, the correlation values suggest that our identified cases are not significantly biased by the magnitude of completeness at different grids.
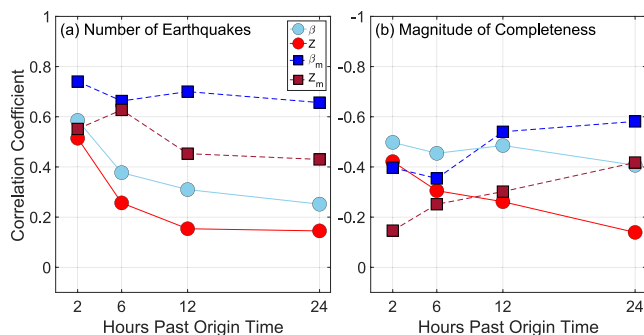


**Figure 11.** Correlation coefficients between triggering occurrence and (a) the number of earthquakes within the grid cell and (b) the magnitude of completeness of earthquakes within the grid cell. Horizontal axis denotes the four time windows.

**Table 3**
*Table of Triggering Results Before and After Removing Aftershocks of Candidate Trigger Earthquakes Using the Knopoff et al. (1982) Spatial Footprint and a 1-Day Temporal Window*

|  | All candidate earthquakes | Aftershocks removed |
|---|---|---|
| Number of candidate | 1,388 | 1,214 |
| Percent of candidates that trigger ($\beta$) | 70 | 68 |
| Percent of candidates that trigger ($Z$) | 60 | 60 |
| Percent of candidates that trigger ($\beta_m$) | 52 | 52 |
| Percent of candidates that trigger ($Z_m$) | 32 | 32 |
| Interevent time in days ($\beta$) | 3.4 | 4 |
| Interevent time in days ($Z$) | 3.9 | 4.5 |
| Interevent time in days ($\beta_m$) | 4.5 | 5.2 |
| Interevent time in days ($Z_m$) | 7.4 | 8.3 |

### 4.2. Resolution

The overlapping $\delta_a$ windows may limit the temporal resolution of triggering types due to the inclusion of seismicity from earlier time windows in later ones. Intensely triggered seismicity or a large moment in a previous window could lead to an identification at a later time window, even if the triggering has ceased. Aftershocks of dynamically triggered earthquakes could contribute to extended cases, but would not impact the identification of instantaneously triggered cases. The detection and localization of local microearthquakes may be challenging due to the coda of passing seismic waves, potentially leading to missed instantaneous cases. Additionally, our procedure may have underestimated the number of instantaneous triggering cases since sporadic earthquakes with low seismicity-rates or magnitudes below $M_c$ may have been missed.

In cases where multiple earthquakes occur within 24 hr and triggering is observed at the grids, we consider each earthquake to have contributed to dynamic triggering, which may overestimate its occurrence. To evaluate the effect of $M \geq 6$ aftershocks of $M \geq 7$ candidate earthquakes on our reported identifications of dynamic triggering, we compare results before and after removing them as candidate events, which might help avoid counting duplicate trigger earthquakes and underestimating recurrence and interevent times.

To remove potential aftershocks of candidate trigger earthquakes, we adopt a spatial window based on Knopoff et al. (1982), which ranges from 100 km for M6 events to 900 km for M8 events. If a smaller candidate event is within 24 hr and falls within the spatial footprint of a larger candidate earthquake, it is considered an aftershock and removed from the candidate trigger list. While the spatial footprint from Knopoff et al. (1982) overestimates the aftershock zone and yields upper limits on recurrence and interevent times, the percentage of candidate earthquakes causing dynamic triggering is largely unaffected by aftershock removal (Table 3), indicating the robustness of our findings. Given the negligible effects of removing the aftershocks, we opt to keep the $M \geq 6$ aftershocks as potential candidate trigger earthquakes when reporting the overall results for completeness.

Our procedure does not distinguish the triggering effects of multiple candidate earthquakes that occur within 24 hr of each other. To investigate whether the occurrence of multiple candidates increases the likelihood of dynamic triggering in southern California, we analyze a 9-year time series that counts the number of global $M \geq 6$ earthquakes in the preceding 24 hr of each candidate earthquake and a binary time series recording triggering incidence identified using the $\beta$-statistic. The correlation between the two time series is insignificant with a coefficient of $-0.02$ (e.g., $\beta$-statistic). Similar insignificant correlations are observed for other statistics ($Z$, $\beta_m$, and $Z_m$). Therefore, we conclude that the presence of multiple candidate earthquakes within 24 hr does not significantly impact the observed triggering patterns.

### 4.3. Statistic Comparison

Various statistics have been used to measure seismicity-rate changes, such as the $\beta$-, $Z$-, and $\gamma$-statistics (Habermann, 1983; Marsan & Nalbant, 2005; Matthews & Reasenberg, 1988). The significance threshold for these statistics can be obtained through their probability distributions assuming random earthquake occurrences (e.g., Wyss & Marsan, 2011). The $Z$-statistic is often preferred over the $\beta$-statistic (e.g., Aiken et al., 2018), but their difference in identifying dynamic triggering is unclear because conventional approaches assume earthquake occurrence as a Poissonian process, which is inaccurate for triggered seismicity.

To compare the $\beta$- and $Z$-statistics (and the $\beta_m$- and $Z_m$-statistics), we compute correlation coefficients between pairs of statistics for each of the 1,388 candidate earthquakes. The resulting correlation coefficients are computed for each time window (Figure S5 in Supporting Information S1) and show that seismicity anomalies identified by the $\beta$- and $Z$-statistics are highly correlated. Similarly, moment-release anomalies identified by the $\beta_m$- and $Z_m$-statistics also have high correlation. The correlation values between seismicity-rate and moment-release anomalies are lower. The results indicate that the choice of test statistic (e.g., $\beta$- or $Z$-statistic) is not crucial for our sampling procedure. Additional details and discussion are described in Supporting Information S1 (Text S3).
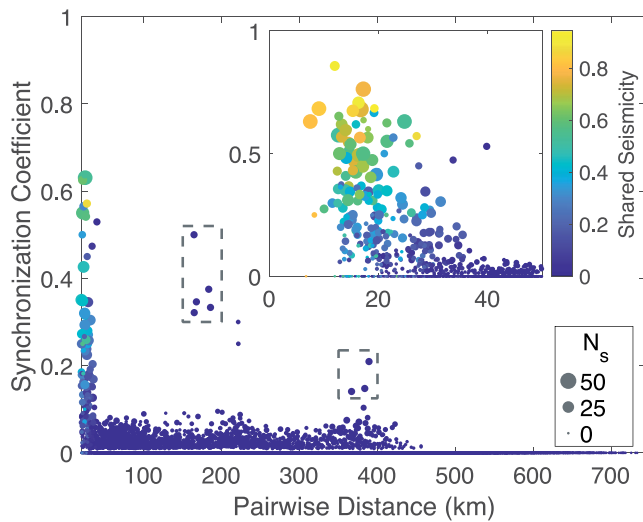
**Figure 12.** Synchronization coefficient versus pairwise grid node distance. Inset displays a zoom-in view for grid nodes that are less than 50 km apart. Marker color shows the fraction of local earthquakes that are shared between overlapping grid cells during the study period. Marker size indicates the number of candidate earthquakes that cause triggering at both grids, $N_s$.

The differences between the seismicity-rate and moment-release anomalies suggest that southern California frequently experiences dynamically triggered seismicity, while earthquakes with significant moment-releases are triggered less often (Section 3.1). For example, the Salton Sea and Coso Geothermal Fields frequently have dynamic triggering in seismicity, but rarely have moment-release anomalies, likely because the thermal production areas are dominated by fragmented faults with small spatial extents (e.g., Cheng & Chen, 2018) limiting the triggered earthquake sizes. Similarly, the immature Ridgecrest fault system may contain more small fault strands (e.g., Ross, Idini, et al., 2019), which may have contributed to the triggering differences in seismicity-rate and moment-release in the region. In contrast, the San Jacinto and Elsinore faults have comparable triggering occurrence for the seismicity-rate and moment-release anomalies. The observed differences in triggering rates of seismicity-rate and moment-release anomalies could be also due to the greater variability in seismic moments since one unit of magnitude difference is equivalent to over one order moment-release difference. To evaluate the effects of moment-release variability of local earthquakes, we have substituted earthquake moment for magnitude in the $\beta_m$ and $Z_m$ calculations at eight grids (Table S5 in Supporting Information S1) and find that using magnitudes would result in small decreases in the triggering rates, leading to greater differences between the seismicity-rate and moment-release anomalies. The results suggest that the large variability in seismic moment is unlikely the cause of the observed statistic differences.

Moment-release anomalies are identified every week on average in southern California using the $\beta_m$- and $Z_m$-statistics and are dominated by the largest earthquakes in the time windows. However, our statistical tests cannot determine whether specific individual earthquakes were dynamically triggered. For simplicity, we convert the moment-anomalies to their equivalent moment magnitudes, remove duplicates from overlapping grid cells and time windows, and find a nominal moment-release anomaly of $M_w$ 3 (Figure S6 in Supporting Information S1). Intriguingly, the $\beta_m$- and $Z_m$-statistics identified six and five cases with equivalent moments above $M_w$ 5, respectively. Apart for one event likely related to the 2010 El Mayor Cucapah earthquake, each case was identified as delayed triggering with delay times from 6 to 24 hr. No obvious foreshock sequences were observed during the delay times upon close inspection of seismicity. Our procedure cannot conclude whether these specific cases were dynamically triggered or not, and the delayed nature hinders rejecting the null hypothesis of random occurrence. Further detailed investigations are warranted in future follow-up studies to understand these unusual $M \geq 5$ cases.

### 4.4. Triggering Scale

To investigate the spatial extent of dynamic triggering, we introduce the synchronization coefficient, $S_{i,j}$, between pairs of grids:

$$S_{i,j} = \frac{N_s}{N_{tot}}, \tag{10}$$

where $i$ and $j$ are two grid indexes, $N_s$ is the number of shared candidate earthquakes that have triggered grids, and $N_{tot}$ is the number of unique candidate earthquakes that have triggered either or both grids. $S_{i,j}$ ranges from 0 to 1 with 1 indicating complete synchronization and 0 indicating no simultaneous dynamic triggering at the two grids during the study period. We calculate $S_{i,j}$ for all pairs of grids and analyze its dependence on the separation distance between the grids.

We hypothesize that high synchronization coefficients reflect common triggering processes between grids, with their separation distance acting as a proxy for the spatial extent of these processes (Figure 12). For example, there is a sharp drop in $S_{i,j}$ beyond a distance of 40 km for seismicity-rate anomalies (e.g., $\beta$-statistic). As the gridding configuration (Section 2.2) results in overlapping cells between adjacent nodes, the 40 km threshold roughly corresponds to two grids. Therefore, the results suggest highly localized triggering responses of seismicity in
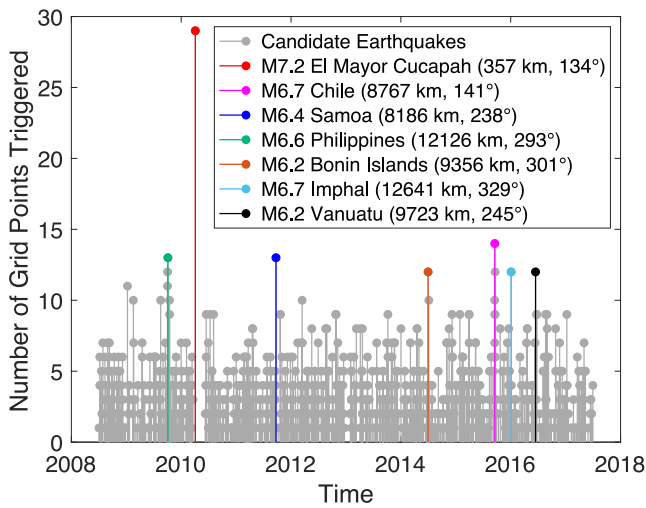
**Figure 13.** Time series of the number of grids triggered after each candidate earthquake ($\beta$-statistic). The legend displays the distance and azimuth from selected example candidates and the centroid of the study area (34.5433°, −117.9895°). Candidate earthquakes within 60 days following the 2010 El Mayor Cucapah earthquake are excluded (Section 2.1).

southern California, occurring over small spatial scales, possibly on the order of 40 km or less. This pattern is also evident in the results obtained using the $Z$-, $\beta_m$-, and $Z_m$-statistics (Figures S8–S10 in Supporting Information S1).

Synchronization coefficients are generally low for grid nodes separated beyond 40 km. However, there are two outlier groups (gray boxes in Figure 12) with pairwise distances over 40 km. The first group, about 175 km apart, is associated with triggering responses from the 2015 M8.3 Illapel earthquake, Chile and its aftershocks, while the second group, around 400 km apart, is due to the 2010 M8.8 Maule earthquake, Chile and its aftershocks. The two groups are likely artifacts resulting from multiple $M \geq 6$ aftershocks within 24 hr being considered triggering despite having overlapping seismicity windows ($\delta_a$). Our results suggest that triggering processes at different faults in southern California are primarily uncorrelated, and the triggering responses are highly heterogeneous. To investigate such processes, a dense network with comparable spatial scales (40 km), such as the Japanese Hi-net (Okada et al., 2004), would be needed to accurately resolve waveform characteristics within each cell.

To investigate the triggering scales, we also examine the number of triggered grids by each candidate earthquake (Figure 13). Results show considerable variation in triggering response among different candidate trigger earthquakes. For example, the 2010 El Mayor Cucapah earthquake triggered seismicity-rate anomalies ($\beta$-statistic) at the most number of grids in southern California, with 29 grids (Figure S7 in Supporting Information S1), even after excluding grids within 50 km of the epicenter, consistent with Ross, Trugman, et al. (2019) and Meng and Peng (2014). The M6.7 aftershock of the 2015 M8.3 Illapel, Chile earthquake is the second most productive trigger earthquake, causing seismicity anomalies at 14 grids. The 2009 M6.6 Philippines earthquake and the 2011 M6.4 Samoa earthquake both correlate with seismicity-rate anomalies at 13 grids. On average, the candidate earthquakes cause triggering at about three grids. These results further confirm that dynamic triggering occurs at local scales, and the triggering responses at different grids are typically independent. Similar plots for the other three statistics ($Z$, $\beta_m$, and $Z_m$) are included in Supporting Information S1 (Figures S11–S13).

## 4.5. Triggering Threshold

We find the triggering thresholds exhibit large spatial heterogeneity and temporal variability (e.g., Figures S14–S21 in Supporting Information S1). The 95th percentile thresholds (e.g., $\beta_{95\%}^a$) for identifying anomalies are generally greater than 2 (e.g., $\beta_{95\%}^a \geq 2$). Spatial patterns of the thresholds do not seem to correlate with seismicity-rates or triggering occurrence. In the 2-hr window, the $\beta_{95\%}^a$ thresholds for the San Jacinto fault, Elsinore fault, and Coso Geothermal Field are relatively high (e.g., Figure S14 in Supporting Information S1), while the Salton Sea Geothermal Field has a lower threshold. The $\beta_{m-95\%}^a$ and $Z_{m-95\%}^a$ thresholds in the 2-hr window show less spatial variation, while exhibiting increased spatial heterogeneity in the 24-hr window. The thresholds evolve significantly over short and long time scales at each grid (e.g., Figure S18 in Supporting Information S1), especially for the $\beta_{95\%}^a$ and $Z_{95\%}^a$ thresholds. These findings suggest that the triggering thresholds are space- and time-dependent, reflecting constantly evolving faulting conditions, and that our data-driven approach effectively accounts for such variability and can identify dynamic triggering cases.

## 4.6. Physical Mechanisms

Earthquake dynamic triggering can be explained by a variety of physical processes (Brodsky & Prejean, 2005; Freed, 2005; Prejean & Hill, 2018). Coulomb failure due to the transient stress perturbation can intuitively explain the instantaneously triggered cases (Gonzalez-Huizar & Velasco, 2011; Hill, 2008; Kilb, 2003): some faults are at critical states, and the dynamic stress pushes them to slip. However, our waveform analyses find no clear correlation between triggering occurrence and the waveform metrics such as peak ground velocity and kinetic energy. This may be because local site effects can cause deformation at the seismogenic depth to differ

from ground motion at the surface (e.g., Hartzell et al., 1997; Parker & Baltay, 2022). However, low-frequency seismic waves may cause similar transient deformation across the crust, supporting that the observed lack of correlation in the low-frequency band is unlikely caused by site effects. The findings agree with previous findings that no simple PGV thresholds can explain dynamic triggering incidences (Freed, 2005; Hill & Prejean, 2015). Intriguingly, the minimum peak ground velocity for instantaneously triggered seismicity and moment-release anomalies appears to be between 0.2 and 0.5 μm/s, a unique feature compared to non-triggering and delayed triggering cases. However, such triggering cases do not always occur when the threshold is reached. Our findings are similar to Kane et al. (2007), who also observed relatively higher PGV values for triggered cases, albeit in a different frequency band.

The 2010 El Mayor Cucapah earthquake triggered widespread responses (Figure S7 in Supporting Information S1), including static and dynamic triggering cases (Meng & Peng, 2014; Miyazawa et al., 2021; Ross, Trugman, et al., 2019). We have investigated the relationships between triggering occurrence and waveform metrics for the earthquake, but find no obvious correlations with the PGV distribution; grids with comparably high PGV values show different triggering responses. Static triggering may have also influenced the triggering response in southern California (Meng & Peng, 2014). To further evaluate the Coulomb failure mechanism, we investigate candidate events that caused dynamic triggering at 10 or more grids, and find no clear patterns. The lack of clear correlation with PGV may be due to different critical states of the faults, requiring different levels of stress perturbations. Additionally, the local stress field may have facilitated triggering for incoming waves from preferred azimuths (Alfaro-Diaz et al., 2020; Gonzalez-Huizar & Velasco, 2011).

Dynamic triggering in southern California may be azimuth-dependent (e.g., Alfaro-Diaz et al., 2020; Fan et al., 2021) For example, Fan et al. (2021) observed a a weak correlation between the triggering occurrence and candidate earthquake back-azimuth as has been observed at the San Jacinto fault and Salton Sea Geothermal Field (Fan et al., 2021). However, triggering can occur for all back-azimuths, indicating the influence of complex local stress fields (orientations). Directly comparing back-azimuth with the triggering pattern remains challenging due to the unresolved complex stress fields at a 40-km resolution in southern California. The findings support that local-scale processes play a significant role in dynamic triggering.

To analyze the characteristics of the triggered seismicity, we have analyzed the Gutenberg-Richter $b$-values (Gutenberg & Richter, 1944) of background and triggered seismicity using a maximum likelihood estimator (Aki, 1965; Goebel et al., 2017) and a $b$-positive estimator (van der Elst, 2021). We take seismicity during the identified triggering time window at a given site as triggered seismicity and the rest of the earthquakes at the site as background seismicity. It is worth noting that our method does not distinguish local earthquakes from dynamically triggered events during the time window. The procedure results in the assumed triggered seismicity also including some background seismicity, which may bias the $b$-value estimates. Here we focus on the triggered seismicity identified by the $\beta$-statistic, and we observe that the triggered seismicity generally has a smaller $b$-value in comparison to that of the background seismicity (Figure S25 in Supporting Information S1). The pattern is consistently observed in estimates obtained using both estimators, albeit the maximum likelihood estimator results in greater differences (0.2–0.4) than the $b$-positive estimator (0.1–0.3). Similar patterns are observed for triggered seismicity identified by the $Z$-, $\beta_m$-, and $Z_m$-statistics. The $b$-value differences suggest that triggered seismicity has a relative abundance of larger events compared to the background, consistent with the common occurrence of seismic-moment anomalies. These findings are also consistent with case studies reported in Fan et al. (2021).

Delayed dynamic triggering is a time-dependent process likely controlled by non-linear mechanisms, including rate-and-state friction, material fatigue, aseismic slip, pore pressure, permeability enhancement, and granular flow (e.g., Brodsky & van der Elst, 2014; Fan et al., 2021; Hill & Prejean, 2015; Johnson & Jia, 2005; Miyazawa et al., 2021; Rivera & Kanamori, 2002; Shelly et al., 2011). Such processes may correlate better with wavefield features such as the frequency content of the passing seismic waves and the duration of intense ground motions (e.g., Pollitz et al., 2012). For example, triggering occurrence seems to relate to the PGV in low frequency bands at Long Valley (Brodsky & Prejean, 2005) and Parkfield (Guilhem et al., 2010). However, our observations of delayed cases in southern California show no correlation with the PGV or kinetic energy (Figures 9 and 10). Furthermore, we find no systematic correlations with the peak frequency or frequency content (Figure 10). These results are consistent with the median spectra reported by Kane et al. (2007), and indicate the need for nonlinear processes to initiate dynamic triggering in the region.

Our analyses of triggering scale show that dynamic triggering is likely governed by conditions operating on spatial scales of tens of kilometers. The localized spatial extent of triggering may help explain the diverse triggering responses, including the possibility that Coulomb failure may be the driver for instantaneous triggering cases. In such cases, small-scale fault patches may be at a wide range of conditions, and some are likely at the critically stressed stage before wave passage. Importantly, the results highlight that local conditions may play a more significant role in the occurrence of triggering than features of the incoming wave, emphasizing the importance of understanding the heterogeneous stress and strength states of faults in southern California.

Models based on experimentally derived rate- and state-dependent fault properties have shown that earthquake production relates to local stress states, and the stressing episodes due to the passing seismic waves may produce clusters of earthquakes in these regions (Dieterich, 1994). Our results suggest a moderate correlation between seismicity-rate anomalies and the total number of earthquakes above completeness at each grid (Figure 11a). The correlation coefficients decrease with $\delta_a$, suggesting that instantaneous triggering cases are likely dominated by linear processes acting upon the heterogeneous stress field, while delayed cases are likely caused by complex nonlinear processes. We also observe strong correlations with moment-anomalies. However, this may be because more seismically active regions can generate larger earthquakes.

The clear evidence of dynamic triggering operating on local spatial scales (∼40 km) suggests that the process is not influenced by the macro-scale tectonic regimes, such as reported by Velasco et al. (2008). However, larger-scale tectonic processes may inhibit dynamic triggering as reported by Harrington and Brodsky (2006), and the conflicting evidence suggests directions for future comparative investigations. Qualitatively, we notice that frequent triggering occurs at the SJF, SSGF, CGF, and the intersection of the San Andreas and San Jacinto faults, where the fault geometries are complex (Chu et al., 2021; Marshall et al., 2022). The geometric complexities may further indicate complex stress fields at those locations (Yang & Hauksson, 2013). While we experimented computing correlations between the triggering occurrence and the surface trace complexity metrics from Chu et al. (2021), we found no obvious correlation. It is possible that the surface traces do not fully reflect the 3D fault geometry and stress field complexities. Future investigations on the relations between earthquake focal mechanisms and triggering occurrence may offer new insights into the physical mechanisms of dynamic triggering processes.

## 5. Conclusions

We have developed a new approach to statistically identify seismicity-rate and moment-release anomalies caused by earthquake dynamic triggering. We apply the method to southern California seismicity from 2008 to 2017 and find

1. The $\beta$- ($\beta_m$-) and Z- ($Z_m$-) statistics identify similar sets of dynamic triggering cases.
2. We conduct comprehensive tests to show that the identified triggering cases are not random.
3. Earthquake dynamic triggering is ubiquitous in southern California; up to 70% of the 1,388 tested global $M \geq 6$ earthquakes may have dynamically triggered seismicity in the region.
4. The Salton Sea Geothermal Field, Coso Geothermal Field, and San Jacinto fault are prone to dynamic triggering.
5. Given the data used, the average frequency of dynamically triggered events in southern California is once every 4 days.
6. Individual grid cells in southern California are triggered infrequently, with intervals ranging from months to years.
7. Evaluating seismicity at different time windows (2, 6, 12, and 24 hr) following a candidate event, we observe that most dynamic triggering occurs with a delay of 6–24 hr.
8. Significant moment-release anomalies occur less often than significant seismicity-rate increases.
9. There is no clear correlation between triggering patterns and the peak ground velocity, peak frequency, kinetic energy, or frequency content.
10. Local fault conditions likely govern dynamic triggering occurrence.

These observations suggest that the majority of the observed triggering cases are likely caused by time-dependent nonlinear mechanisms operating on local scales.

## Data Availability Statement

The earthquake catalogs used in this study are from the International Seismological Centre (ISC) bulletin (International Seismological Centre, 2022) and the Southern California Earthquake Data Center (Quake Template Matching catalog; Ross, Trugman, et al., 2019). The facilities of IRIS Data Services, and specifically the IRIS Data Management Center, were used for access to the seismic waveforms and the ISC catalog, related metadata, and/or derived products used in this study. IRIS Data Services are funded through the Seismological Facilities for the Advancement of Geoscience and EarthScope (SAGE) Proposal of the National Science Foundation (NSF) under Cooperative Agreement EAR-1261681. The seismic data were downloaded using ObsPy (Beyreuther et al., 2010) and the International Federation of Digital Seismograph Networks (FDSN) web services. The reported triggering cases are included in a Data Set S1.

## References

Abercrombie, R. E., & Mori, J. (1996). Occurrence patterns of foreshocks to large earthquakes in the western United States. *Nature*, *381*(6580), 303–307. https://doi.org/10.1038/381303a0

Aiken, C., Meng, X., & Hardebeck, J. (2018). Testing for the 'predictability' of dynamically triggered earthquakes in the Geysers geothermal field. *Earth and Planetary Science Letters*, *486*, 129–140. https://doi.org/10.1016/j.epsl.2018.01.015

Aiken, C., & Peng, Z. (2014). Dynamic triggering of microearthquakes in three geothermal/volcanic regions of California. *Journal of Geophysical Research: Solid Earth*, *119*(9), 6992–7009. https://doi.org/10.1002/2014JB011218

Aki, K. (1965). Maximum likelihood estimate of b in the forumla log n = a - bm and its confidence limits. *Bulletin of the Earthquake Research Institute*, *43*, 237–239.

Alfaro-Diaz, R., Velasco, A. A., Pankow, K. L., & Kilb, D. (2020). Optimally oriented remote triggering in the coso geothermal region. *Journal of Geophysical Research: Solid Earth*, *125*(8), e2019JB019131. https://doi.org/10.1029/2019jb019131

Beyreuther, M., Barsch, R., Krischer, L., Megies, T., Behr, Y., & Wassermann, J. (2010). Obspy: A python toolbox for seismology. *Seismological Research Letters*, *81*(3), 530–533. https://doi.org/10.1785/gssrl.81.3.530

Bosl, W., & Nur, A. (2002). Aftershocks and pore fluid diffusion following the 1992 landers earthquake. *Journal of Geophysical Research*, *107*(B12), ESE17-1–ESE17-12. https://doi.org/10.1029/2001JB000155

Brodsky, E. E., & Prejean, S. G. (2005). New constraints on mechanisms of remotely triggered seismicity at Long Valley Caldera. *Journal of Geophysical Research*, *110*(B4). https://doi.org/10.1029/2004JB003211

Brodsky, E. E., & van der Elst, N. J. (2014). The uses of dynamic earthquake triggering. *Annual Review of Earth and Planetary Sciences*, *42*(1), 317–339. https://doi.org/10.1146/annurev-earth-060313-054648

Buurman, H., & West, M. E. (2010). *Seismic precursors to volcanic explosions during the 2006 eruption of Augustine Volcano: Chapter 2 in the 2006 eruption of Augustine Volcano, Alaska (Technical report no. 1769-2)*. U.S. Geological Survey. (ISSN: 2330-7102 Publication Title: Professional Paper). https://doi.org/10.3133/pp17692

Cheng, Y., & Chen, X. (2018). Characteristics of seismicity inside and outside the Salton Sea geothermal field. *Bulletin of the Seismological Society of America*, *108*(4), 1877–1888. https://doi.org/10.1785/0120170311

Chu, S. X., Tsai, V. C., Trugman, D. T., & Hirth, G. (2021). Fault interactions enhance high-frequency earthquake radiation. *Geophysical Research Letters*, *48*(20), e2021GL095271. https://doi.org/10.1029/2021GL095271

Dieterich, J. (1994). A constitutive law for rate of earthquake production and its application to earthquake clustering. *Journal of Geophysical Research*, *99*(B2), 2601–2618. https://doi.org/10.1029/93JB02581

Dziewonski, A. M., & Anderson, D. L. (1981). Preliminary reference Earth model. *Physics of the Earth and Planetary Interiors*, *25*(4), 297–356. https://doi.org/10.1016/0031-9201(81)90046-7

Fan, W., Barbour, A. J., Cochran, E. S., & Lin, G. (2021). Characteristics of frequent dynamic triggering of microearthquakes in Southern California. *Journal of Geophysical Research: Solid Earth*, *126*(1). https://doi.org/10.1029/2020JB020820

Fan, W., Okuwaki, R., Barbour, A. J., Huang, Y., Lin, G., & Cochran, E. S. (2022). Fast rupture of the 2009 Mw 6.9 Canal de Ballenas earthquake in the Gulf of California dynamically triggers seismicity in California. *Geophysical Journal International*, *230*(1), 528–541. https://doi.org/10.1093/gji/ggac059

Felzer, K. R., & Brodsky, E. E. (2006). Decay of aftershock density with distance indicates triggering by dynamic stress. *Nature*, *441*(7094), 735–738. https://doi.org/10.1038/nature04799

Fiedler, B., Hainzl, S., Zöller, G., & Holschneider, M. (2018). Detection of Gutenberg–Richter b-value changes in earthquake time Series. *Bulletin of the Seismological Society of America*, *108*(5A), 2778–2787. https://doi.org/10.1785/0120180091

Field, E. H., Arrowsmith, R. J., Biasi, G. P., Bird, P., Dawson, T. E., Felzer, K. R., et al. (2014). Uniform California Earthquake Rupture Forecast, Version 3 (UCERF3)—The Time-Independent Model. *Bulletin of the Seismological Society of America*, *104*(3), 1122–1180. https://doi.org/10.1785/0120130164

Freed, A. M. (2005). Earthquake triggering by static, dynamic, and postseismic stress transfer. *Annual Review of Earth and Planetary Sciences*, *33*(1), 335–367. https://doi.org/10.1146/annurev.earth.33.092203.122505

Goebel, T. H., Kwiatek, G., Becker, T. W., Brodsky, E. E., & Dresen, G. (2017). What allows seismic events to grow big?: Insights from b-value and fault roughness analysis in laboratory stick-slip experiments. *Geology*, *45*(9), 815–818. https://doi.org/10.1130/G39147.1

Gomberg, J. (1996). Stress/strain changes and triggered seismicity following the Mw 7.3 Landers, California earthquake. *Journal of Geophysical Research*, *101*(B1), 751–764. https://doi.org/10.1029/95JB03251

Gomberg, J., & Johnson, P. (2005). Dynamic triggering of earthquakes. *Nature*, *437*(7060), 830. https://doi.org/10.1038/437830a

Gomberg, J., Reasenberg, P., Bodin, P. l., & Harris, R. (2001). Earthquake triggering by seismic waves following the landers and hector mine earthquakes. *Nature*, *411*(6836), 462–466. https://doi.org/10.1038/35078053

Gonzalez-Huizar, H., & Velasco, A. A. (2011). Dynamic triggering: Stress modeling and a case study. *Journal of Geophysical Research*, *116*(B2), B02304. https://doi.org/10.1029/2009JB007000

Guilhem, A., Peng, Z., & Nadeau, R. M. (2010). High-frequency identification of non-volcanic tremor triggered by regional earthquakes. *Geophysical Research Letters*, *37*(16). https://doi.org/10.1029/2010GL044660

Gutenberg, B., & Richter, C. (1944). Frequency of earthquakes in California. *Bulletin of the Seismological Society of America*, *34*(4), 185–188. https://doi.org/10.1785/bssa0340040185

Habermann, R. E. (1983). Teleseismic detection in the Aleutian Island Arc. *Journal of Geophysical Research*, *88*(B6), 5056–5064. https://doi.org/10.1029/JB088iB06p05056

Harrington, R. M., & Brodsky, E. E. (2006). The absence of remotely triggered seismicity in Japan. *Bulletin of the Seismological Society of America*, *96*(3), 871–878. https://doi.org/10.1785/0120050076

Harris, R. A., & Simpson, R. W. (1992). Changes in static stress on southern California faults after the 1992 landers earthquake. *Nature*, *360*(6401), 251–254. https://doi.org/10.1038/360251a0

Hartzell, S., Cranswick, E., Frankel, A., Carver, D., & Meremonte, M. (1997). Variability of site response in the Los Angeles urban area. *Bulletin of the Seismological Society of America*, *87*(6), 1377–1400. https://doi.org/10.1785/BSSA0870061377

Hill, D. P. (2008). Dynamic stresses, coulomb failure, and remote triggering. *Bulletin of the Seismological Society of America*, *98*(1), 66–92. https://doi.org/10.1785/0120070049

Hill, D. P., & Prejean, S. G. (2015). 4.11 - Dynamic triggering. In G. Schubert (Ed.), *Treatise on geophysics* (2nd ed., pp. 273–304). Elsevier. https://doi.org/10.1016/B978-0-444-53802-4.00078-6

Inbal, A., Ampuero, J.-P., & Avouac, J.-P. (2017). Locally and remotely triggered aseismic slip on the central San Jacinto Fault near Anza, CA, from joint inversion of seismicity and strainmeter data. *Journal of Geophysical Research: Solid Earth*, *122*(4), 3033–3061. https://doi.org/10.1002/2016JB013499

International Seismological Centre. (2022). On-line bulletin. [Computer software manual]. https://doi.org/10.31905/D808B830

Johnson, P. A., & Jia, X. (2005). Nonlinear dynamics, granular media and dynamic earthquake triggering. *Nature*, *437*(7060), 871–874. https://doi.org/10.1038/nature04015

Kane, D. L., Kilb, D., Berg, A. S., & Martynov, V. G. (2007). Quantifying the remote triggering capabilities of large earthquakes using data from the ANZA Seismic Network catalog (southern California). *Journal of Geophysical Research*, *112*(B11), B11302. https://doi.org/10.1029/2006JB004714

Kilb, D. (2003). A strong correlation between induced peak dynamic Coulomb stress change from the 1992 M7.3 Landers, California, earthquake and the hypocenter of the 1999 M7.1 Hector Mine, California, earthquake. *Journal of Geophysical Research*, *108*(B1), ESE3–1–ESE3–7. https://doi.org/10.1029/2001JB000678

Kilb, D., Gomberg, J., & Bodin, P. (2000). Triggering of earthquake aftershocks by dynamic stresses. *Nature*, *408*(6812), 570–574. https://doi.org/10.1038/35046046

Knopoff, L, Kagan, Y. Y., & Knopoff, R. (1982). b values for foreshocks and aftershocks in real and simulated earthquake sequences. *Bulletin of the Seismological Society of America*, *72*(5), 1663–1676. https://doi.org/10.1785/BSSA0720051663

Li, C, Peng, Z., Yao, D., Meng, X., & Zhai, Q. (2022). Temporal changes of seismicity in Salton Sea geothermal field due to distant earthquakes and geothermal productions. *Geophysical Journal International*, *232*(1), 287–299. https://doi.org/10.1093/gji/ggac324

Marsan, D., & Nalbant, S. S. (2005). Methods for measuring seismicity rate changes: A review and a study of how the Mw7.3 Landers earthquake affected the aftershock sequence of the Mw6.1 Joshua tree earthquake. *Pure and Applied Geophysics*, *162*(6), 1151–1185. https://doi.org/10.1007/s00024-004-2665-4

Marshall, S., Plesch, A., Shaw, J., & Nicholson, C. (2022). SCEC Community Fault Model (CFM). [Dataset]. Zenodo. https://doi.org/10.5281/zenodo.5899364

Matthews, M. V., & Reasenberg, P. A. (1988). Statistical methods for investigating quiescence and other temporal seismicity patterns. *Pure and Applied Geophysics*, *126*(2), 357–372. https://doi.org/10.1007/BF00879003

Meng, X., & Peng, Z. (2014). Seismicity rate changes in the Salton Sea geothermal field and the San Jacinto Fault Zone after the 2010 Mw 7.2 El Mayor-Cucapah earthquake. *Geophysical Journal International*, *197*(3), 1750–1762. https://doi.org/10.1093/gji/ggu085

Miyazawa, M., Brodsky, E. E., & Guo, H. (2021). Dynamic earthquake triggering in Southern California in high resolution: Intensity, time decay, and regional variability. *AGU Advances*, *2*(2), e2020AV000309. https://doi.org/10.1029/2020AV000309

Moutote, L., Marsan, D., Lengliné, O., & Duputel, Z. (2021). Rare occurrences of non-cascading foreshock activity in Southern California. *Geophysical Research Letters*, *48*(7), e2020GL091757. https://doi.org/10.1029/2020GL091757

Ogata, Y. (1988). Statistical models for earthquake occurrences and residual analysis for point processes. *Journal of the American Statistical Association*, *83*(401), 9–27. https://doi.org/10.1080/01621459.1988.10478560

Okada, Y., Kasahara, K., Hori, S., Obara, K., Sekiguchi, S., Fujiwara, H., & Yamamoto, A. (2004). Recent progress of seismic observation networks in Japan—Hi-net, F-net, K-net and Kik-net. *Earth Planets and Space*, *56*(8), xv–xxviii. https://doi.org/10.1186/BF03353076

Pankow, K. L., & Kilb, D. (2020). Going beyond rate changes as the sole indicator for dynamic triggering of earthquakes. *Scientific Reports*, *10*(1), 4120. https://doi.org/10.1038/s41598-020-60988-2

Parker, G. A., & Baltay, A. S. (2022). Empirical map-based nonergodic models of site response in the greater Los Angeles area. *Bulletin of the Seismological Society of America*, *112*(3), 1607–1629. https://doi.org/10.1785/0120210175

Parsons, T., & Dreger, D. S. (2000). Static-stress impact of the 1992 landers earthquake sequence on nucleation and slip at the site of the 1999 m=7.1 hector mine earthquake, southern California. *Geophysical Research Letters*, *27*(13), 1949–1952. https://doi.org/10.1029/1999GL011272

Pollitz, F. F., Stein, R. S., Sevilgen, V., & Bürgmann, R. (2012). The 11 April 2012 east Indian Ocean earthquake triggered large aftershocks worldwide. *Nature*, *490*(7419), 250–253. https://doi.org/10.1038/nature11504

Prejean, S. G., Hill, D. P., Brodsky, E. E., Hough, S. E., Johnston, M. J. S., Malone, S. D., & Richards-Dinger, K. B. (2004). Remotely triggered seismicity on the United States West Coast following the Mw 7.9 Denali fault earthquake. *Bulletin of the Seismological Society of America*, *94*(6B), S348–S359. https://doi.org/10.1785/0120040610

Prejean, S. G., & Hill, D. P. (2018). The influence of tectonic environment on dynamic earthquake triggering: A review and case study on Alaskan volcanoes. *Tectonophysics*, *745*, 293–304. https://doi.org/10.1016/j.tecto.2018.08.007

Rivera, L., & Kanamori, H. (2002). Spatial heterogeneity of tectonic stress and friction in the crust. *Geophysical Research Letters*, *29*(6), 12–1–12–4. https://doi.org/10.1029/2001GL013803

Ross, Z. E., Idini, B., Jia, Z., Stephenson, O. L., Zhong, M., Wang, X., et al. (2019). Hierarchical interlocked orthogonal faulting in the 2019 Ridgecrest earthquake sequence. *Science*, *366*(6463), 346–351. https://doi.org/10.1126/science.aaz0109

Ross, Z. E., Trugman, D. T., Hauksson, E., & Shearer, P. M. (2019). Searching for hidden earthquakes in Southern California. *Science*, *364*(6442), 767–771. https://doi.org/10.1126/science.aaw6888

Shearer, P. M. (2012a). Self-similar earthquake triggering, Båth's law, and foreshock/aftershock magnitudes: Simulations, theory, and results for southern California. *Journal of Geophysical Research*, *117*(B6). https://doi.org/10.1029/2011JB008957

Shearer, P. M. (2012b). Space-time clustering of seismicity in California and the distance dependence of earthquake triggering. *Journal of Geophysical Research*, *117*(B10). https://doi.org/10.1029/2012JB009471

Shearer, P. M., Abercrombie, R. E., & Trugman, D. T. (2022). Improved stress drop estimates for m 1.5 to 4 earthquakes in southern California from 1996 to 2019. *Journal of Geophysical Research: Solid Earth*, *127*(7), e2022JB024243. https://doi.org/10.1029/2022JB024243

Shelly, D. R., Peng, Z., Hill, D. P., & Aiken, C. (2011). Triggered creep as a possible mechanism for delayed dynamic triggering of tremor and earthquakes. *Nature Geoscience*, *4*(6), 384–388. https://doi.org/10.1038/ngeo1141

Stark, M. A., & Davis, S. D. (1996). Remotely triggered microearthquakes at the Geysers Geothermal Field, California. *Geophysical Research Letters*, *23*(9), 945–948. https://doi.org/10.1029/96GL00011

Thomson, D. (1982). Spectrum estimation and harmonic analysis. *Proceedings of the IEEE*, *70*(9), 1055–1096. https://doi.org/10.1109/PROC.1982.12433

Trugman, D. T., & Ross, Z. E. (2019). Pervasive foreshock activity across southern California. *Geophysical Research Letters*, *46*(15), 8772–8781. https://doi.org/10.1029/2019GL083725

Uchide, T., Horikawa, H., Nakai, M., Matsushita, R., Shigematsu, N., Ando, R., & Imanishi, K. (2016). The 2016 Kumamoto–Oita earthquake sequence: Aftershock seismicity gap and dynamic triggering in volcanic areas. *Earth Planets and Space*, *68*(1), 1–10. https://doi.org/10.1186/s40623-016-0556-4

Utsu, T. (1961). A statistical study on the occurrence of aftershocks. *Geophysical Magazine*, *30*, 521–605.

van der Elst, N. J. (2021). B-positive: A robust estimator of aftershock magnitude distribution in transiently incomplete catalogs. *Journal of Geophysical Research: Solid Earth*, *126*(2), e2020JB021027. https://doi.org/10.1029/2020JB021027

van der Elst, N. J., & Brodsky, E. E. (2010). Connecting near-field and far-field earthquake triggering to dynamic strain. *Journal of Geophysical Research*, *115*(B7), B07311. https://doi.org/10.1029/2009JB006681

Velasco, A. A., Hernandez, S., Parsons, T., & Pankow, K. (2008). Global ubiquity of dynamic earthquake triggering. *Nature Geoscience*, *1*(6), 375–379. https://doi.org/10.1038/ngeo204

Wiemer, S. (2000). Minimum magnitude of completeness in earthquake catalogs: Examples from Alaska, the Western United States, and Japan. *Bulletin of the Seismological Society of America*, *90*(4), 859–869. https://doi.org/10.1785/0119990114

Wyss, M., & Marsan, D. (2011). *Seismicity rate changes*. Community Online Resource for Statistical Seismicity Analysis. https://doi.org/10.5078/CORSSA-25837590

Yang, W., & Hauksson, E. (2013). The tectonic crustal stress field and style of faulting along the Pacific North America plate boundary in southern California. *Geophysical Journal International*, *194*(1), 100–117. https://doi.org/10.1093/gji/ggt113

Yoshida, S. (2016). Earthquakes in Oita triggered by the 2016 M7.3 Kumamoto earthquake. *Earth Planets and Space*, *68*(1), 176. https://doi.org/10.1186/s40623-016-0552-8